

Nanoscale Rheology and Anisotropic Diffusion Using Single Gold Nanorod Probes

Mehdi Molaei, Ehsan Atefi, and John C. Crocker*

*Chemical and Biomolecular Engineering, University of Pennsylvania,
220 South 33rd Street, Philadelphia, Pennsylvania 19104, USA* (Received 30 September 2017; revised manuscript received 4 January 2018; published 15 March 2018)

The complex rotational and translational Brownian motion of anisotropic particles depends on their shape and the viscoelasticity of their surroundings. Because of their strong optical scattering and chemical versatility, gold nanorods would seem to provide the ultimate probes of rheology at the nanoscale, but the suitably accurate orientational tracking required to compute rheology has not been demonstrated. Here we image single gold nanorods with a laser-illuminated dark-field microscope and use optical polarization to determine their three-dimensional orientation to better than one degree. We convert the rotational diffusion of single nanorods in viscoelastic polyethylene glycol solutions to rheology and obtain excellent agreement with bulk measurements. Extensions of earlier models of anisotropic translational diffusion to three dimensions and viscoelastic fluids give excellent agreement with the observed motion of single nanorods. We find that nanorod tracking provides a uniquely capable approach to microrheology and provides a powerful tool for probing nanoscale dynamics and structure in a range of soft materials.

DOI: [10.1103/PhysRevLett.120.118002](https://doi.org/10.1103/PhysRevLett.120.118002)

The Brownian motion of embedded tracers has been applied to determining the viscoelasticity of soft materials and microscopic objects via passive microrheology for more than two decades. Typically, dynamic light scattering [1–4] or image-based particle tracking [3,5–9] is used to measure the tracers' mean-squared displacement (MSD), which is then converted to the dynamic shear modulus via a generalized Stoke-Einstein relation (GSER) [1,2,4,10]. Pioneering work by Cheng and Mason [11] showed that the rotational diffusion of anisotropic micron-scale particles can also be used to quantify the rheology via a rotational GSER, and later it was demonstrated using depolarized dynamic light scattering [12,13]. Multiple imaging-based rotational tracking methods have since been reported [14–18]; however, they do not appear well suited to microrheology. While the use of anisotropic nanoparticle tracers would greatly facilitate the application of this approach to stiffer materials and much smaller length and time scales than possible with larger tracers, microrheology places stringent requirements on the accuracy of the tracer's inferred mean-squared displacement. Indeed, despite several reports of gold nanorod (GNR) rotational tracking using imaging [19–31] and depolarized scattering [32–36], no one has demonstrated the use of GNRs to accurately measure the rheology of a viscoelastic material. Moreover, no models of the complex anisotropic translational diffusion [32,33,37] that these particles would execute in a viscoelastic material, or its coupling to the rotational diffusion, have been reported or validated.

Here, we study the rotational and translational Brownian motion of single GNRs using a laser-illuminated dark-field microscope modified to simultaneously record two

orthogonally polarized images. A polarimetric analysis, based upon a nano-optical model of the GNR, enables the accurate determination of the rods' three-dimensional orientation to better than one degree at up to several thousand frames per second. The rotational diffusion motion quantified by a mean-squared angular displacement can be quantitatively converted into a dynamic shear modulus via a generalized Stokes-Einstein relation. We demonstrate this “nanorheology” approach in concentrated viscoelastic solutions of polyethylene glycol polymer, extending passive microrheology down to 100 nm length and single attoliter (10^{-18} l) volume scales. Moreover, we extend an earlier study [37] of two-dimensional anisotropic translational diffusion [38] in Newtonian fluids to the unbounded, three-dimensional and the viscoelastic cases and find that it accurately reproduces the observed motion of single isolated nanorods.

GNRs are ideal orientation probes, since their surface plasmon resonance [22] depends on their relative orientation with respect to the external electric field [39] and their scattered light is thus strongly polarized [26,40]. Previous studies [26,39,40] have shown that far-field scattered light of a single GNR can be modeled by the electric field emitted from three independent and orthogonal principal dipoles, with the dipole aligned along the rod's long axis being predominant. We computed the strength of these principal dipoles using the discrete dipole approximation method [41–44] (see Supplemental Material Sec. I.1 for details [45]). We image the particles using a custom-built dark-field microscope that focuses a single mode, 300 mW diode pumped solid state laser ($\lambda = 670$ nm) in the back aperture of a high-NA, oil-immersion objective to produce

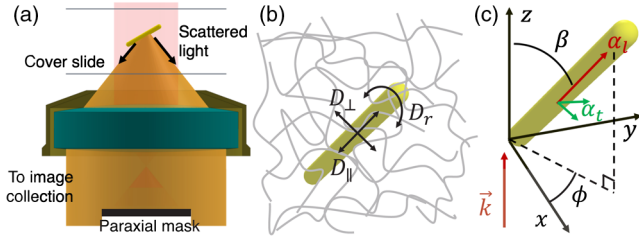


FIG. 1. (a) GNR scattering and imaged by a dark-field microscope. (b) GNR embedded in viscoelastic polymer solution. (c) Coordinate system of the GNR defined by polar β and azimuthal angles ϕ .

a small, collimated Gaussian beam in the specimen [Fig. 1(a)]. We took advantage of the polarization sensitivity of GNR scattering by illuminating the rod with a circularly polarized laser beam and splitting the scattered light into two images on the same camera detector, corresponding to two orthogonal linear polarization channels [45]. The integrated intensity of the GNR images in these two channels is a function of the GNR orientation, specifically, its polar angle β and azimuthal angle ϕ [Fig. 1(c)]. We use a semianalytic physical optics model to compute the expected intensities in our high-numerical-aperture microscope. Inverting these periodic functions maps the inferred position of the rod's orientation into a single octant domain of the unit sphere. While this precludes determining the absolute spatial orientation of the rod, it does allow the angular mean-squared displacement, needed for microrheology, to be reliably determined.

To demonstrate the angular tracking capability of the imaging system, we first studied the motion of GNRs ($20 \times 100 \text{ nm}^2$) in pure glycerol. The intensity of the scattering light in the x and y channels and the total intensity are shown as functions of the time in Figs. 2(a) and 2(b). Figure 2(c) shows the inferred polar and azimuthal angles of a single GNR versus the time. As expected, the inferred GNR orientation, as shown in Fig. 2(d), fully explores the available octant of a unit sphere. Typical images of the GNR at different orientations at selected times are shown in Fig. 2(f). Tracking the centroid position of the GNR over time [Fig. 2(g)] indicates that translational Brownian motion of the GNR is small enough that rods do not go out of focus during image collection. The shape of the distribution of polar angles and azimuthal angles over 10^5 image pairs is consistent with the GNR exploring all orientations randomly to within statistical sampling [Fig. 2(h)], confirming the accuracy of our polarimetric analysis [46–52].

The mean-squared angular displacement (MSAD), $\text{MSAD} = \langle |u(t + \tau) - u(t)|^2 \rangle_t$, is bounded by the direction vector being limited to the unit sphere, leading to a single exponential crossover with an asymptote of 2, $\langle -\Delta \hat{u}^2(t) \rangle = 2[1 - (1 - \varepsilon_r^2) \exp(-2D_r t)]$, where D_r is the rotational diffusion coefficient and ε_r is the measurement error in

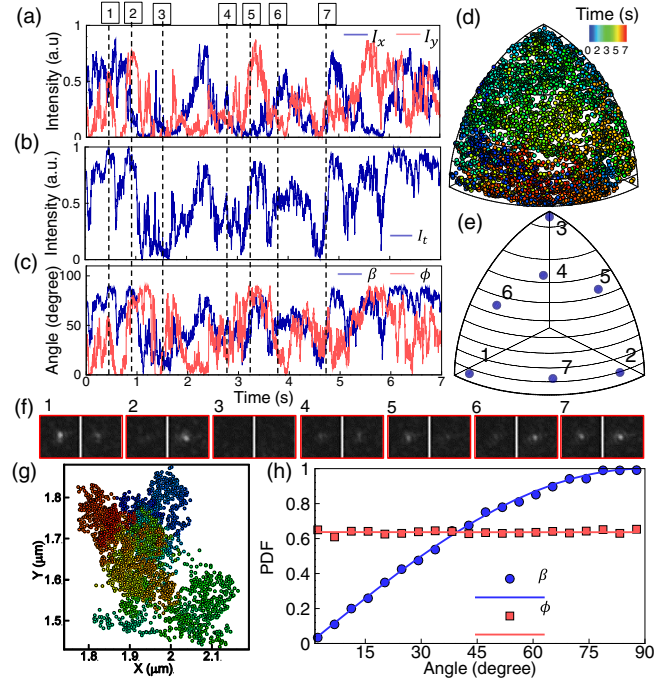


FIG. 2. Integrated intensity of a GNR in glycerol in orthogonal x and y polarization images (a), with the corresponding sum of intensities (b) and the inferred orientation angles (c). Time-dependent 3D GNR orientation mapped into a single octant (d). Orientations of selected time points (1–7) marked in (e), corresponding image pairs ($1.6 \times 1.6 \mu\text{m}^2$) in (f). Trajectory (g) of the GNR showing translational motion. Frequency distributions of orientation angles (h) from 10^5 image pairs (symbols) match a random orientation model (curves).

the orientation vector [14,53,54] [Fig. S5(a)]. With unit vectors mapped to an octant, a similar effect occurs; Monte Carlo (MC) simulations [45] show that the resulting MSAD is well described empirically by a stretched exponential function with an asymptote of 0.5:

$$\langle |\Delta \hat{u}^2(t)| \rangle = \frac{1}{2} \{ 1 - (1 - \varepsilon_r^2) \exp[-(\kappa D_r t)^\zeta] \}, \quad (1)$$

where $\kappa = 1.6$ and $\zeta = 0.95$ are constants [Fig. 3(a)]. Equation (1) compares favorably to the MSAD determined for single GNRs in pure glycerol [Fig. 3(b)]. Fitting yields a rotational diffusion constant $D_r = 3.5 \text{ rad}^2/\text{s}$ and an estimated angular measurement uncertainty $\varepsilon_r^2 = 2.5 \times 10^{-4} \text{ rad}^2$, better than 1° directional precision. We also determined the translational diffusion coefficient by fitting to the short lag time data from centroid-based particle tracking [53] [Fig. S5(c)]: $\langle \Delta r_{xy}^2 \rangle = 4D_t t + 4\varepsilon_r^2$. This yields a value of $D_t = 0.007 \mu\text{m}^2/\text{s}$ and a position uncertainty of $\sim 9 \text{ nm}$.

The theoretical prediction of translational and rotational diffusion coefficients for a rod (in the lab frame) are $D_r = [(3KT)/(\pi\eta l^3)][\ln\rho + C_r(\rho)]$ and $D_t = [(KT)/(3\pi\eta l)]$

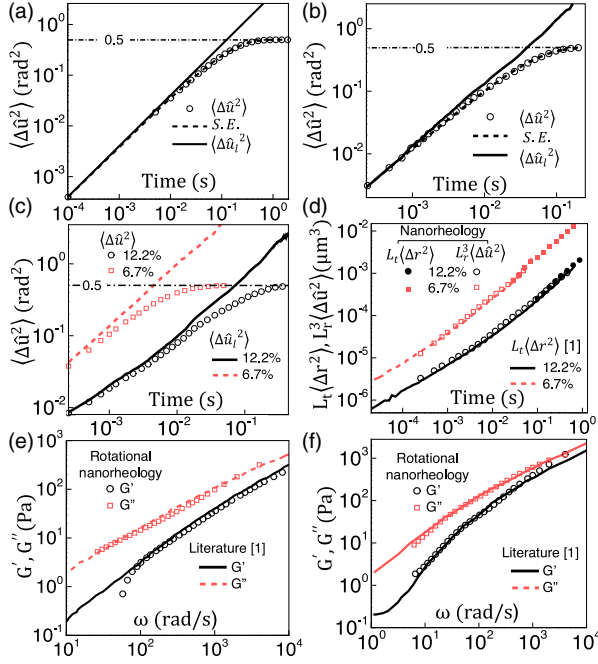


FIG. 3. MSADs of simulated (a) and measured (b) GNR in glycerol (circles), stretched exponential fit (dashed line), and unbounded MSAD (curve). Measured MSADs (c) of a GNR in 200 kDa PEO, 6.7% w/w (squares) and 12.2% w/w (circles). (d) Scaled unbound MSAD (open symbols), translational MSD (closed circles) of the GNR, and rescaled microsphere MSD [1] (lines) at two PEO concentrations. Storage and loss moduli for the PEO solution obtained from GNR rotational nanorheology (symbols) and literature microrheology [1] (lines) at 6.7% w/w (e) and 12.2% w/w (f).

$[\ln \rho + C_r(\rho)]$, where K and T are the Boltzmann constant and temperature, respectively, l and d are the length and diameter, respectively, of the rod, and C_r and C_t are, respectively, the rotational and translational drag coefficient correction factors which are a function of the aspect ratio ρ and the shape of the rod ends [18,55,56]. The ratio of the translational to the rotational diffusion coefficients is only a function of the geometry of the GNR: $(D_t/D_r) = l^2 f(\rho)$. Electron microscopy shows that the rods have a consistent 20 nm diameter and lengths of 100 ± 11 nm; data are shown in Supplemental Material [45]. Using a spherocylinder model and assuming the rods are stripped of their CTAB ligands in neat glycerol, the length of the single GNR tracer is inferred to be $l = 107 \pm 2$ nm, and the viscosity of the solution can be estimated as $\eta = 1.26$ Pa s, in excellent agreement with the expected value of 1.29 Pa s, for pure glycerol at 21 ± 1.5 °C.

The rotational diffusion of a nanorod in a viscoelastic material has been described by a Langevin torque equation $I_r \dot{\Omega}(t) = \Gamma_r(t) - \int_0^t \tilde{\xi}_r(t-\tau) \Omega(\tau) d\tau$, where Ω is the angular velocity of the nanorod, Γ_r is the thermal driving torque, and $\tilde{\xi}_r$ is the rotational memory function [11]. Mason *et al.* have shown that the solution of this equation is similar to

that for the translational Langevin equation [3]. Taking the Laplace transform of the Langevin equation, applying the principles of causality and thermal energy equipartition, and neglecting the inertia term, the Laplace transform of the angular velocity will be $\langle \tilde{v}(0) \tilde{v}(s) \rangle = k_B T / \tilde{\xi}_r(s)$. Taking the GNR as a spherocylinder leads to the Laplace transform of the rotational memory function to be $\tilde{\xi}_r(s) = \frac{1}{3} \pi l^3 \tilde{\eta}(s) / [\ln(\rho) + C_r]$, where $\tilde{\eta}(s)$ is the frequency-dependent viscosity. Replacing $\langle \tilde{v}(0) \tilde{v}(s) \rangle$ with $(s^2/2) \langle \Delta \tilde{u}_r^2(s) \rangle$ leads to the rotational generalized Stokes-Einstein relation (RGSER) for the GNR

$$\tilde{G}(s) = s \tilde{\eta}(s) = \frac{6k_B T}{\pi s l^3 \langle \Delta \tilde{u}_r^2(s) \rangle} [\ln \rho + C_r], \quad (2)$$

where $\Delta \tilde{u}_r^2(s)$ is the Laplace transform of an MSAD, $\langle \Delta \tilde{u}_r^2(t) \rangle$, that unlike $\langle \Delta \hat{u}^2(t) \rangle$ is unbounded in magnitude at a long lag time. We developed an approach that computes a lag-time-independent mapping between these two bounded and unbounded MSADs by inverting Eq. (1), which leads to $\langle \Delta \tilde{u}_r^2(t) \rangle = 4D_r t = (4/k) \{ \ln[1/(1 - 2\langle \Delta \hat{u}^2(t) \rangle)] \}^{1/\zeta}$. We validated this procedure using simulated trajectories of tracer beads in different model viscoelastic fluids using a method developed by Khan and Mason [50]; see Supplemental Material Sec. I.7 [45]. This procedure has the expected effect of linearizing the bounded MSAD of GNR in the glycerol solution; see Fig. 3(b). A limitation of this approach is the amplification of uncertainties in $\langle \Delta \hat{u}^2(t) \rangle$ for lag times longer than the rod's Brownian tumbling time, which limits the usefulness of this method as the bounded MSAD approaches its asymptotic values.

To demonstrate the feasibility of using Eq. (2) to measure nondiffusive Brownian motion and viscoelasticity with single GNRs, we suspended rods in an aqueous polyethylene oxide (PEO) solution (200 K molecular weight, 6.7% and 12.2% w/w), previously employed in a microrheology study by Dasgupta *et al.* [1]. In both samples, the diameter of the rods is larger than the mesh sizes of the entangled polymer solutions at these concentrations (see Supplemental Material for more details of the polymer characteristics [45]). Measured bounded MSADs, shown by symbols in Fig. 3(c), were remapped to unbounded MSADs, shown in Fig. 3(c) by lines.

To validate our tracking results, we can compare them to those of the earlier microsphere study using the same viscoelastic sample, by rescaling the MSDs as $L_t \langle \Delta \tilde{r}^2(s) \rangle$ and MSADs with $L_r^3 \langle \Delta \tilde{u}_r^2(s) \rangle$, where L_t and L_r are, respectively, the translational and rotational effective length of probes derived from equating $\tilde{G}(s) = s \tilde{\eta}(s) = [(2k_B T) / (\pi s L_r^3 \langle \Delta \tilde{u}_r^2(s) \rangle)] = [(2k_B T) / (\pi s L_t \langle \Delta \tilde{r}^2(s) \rangle)]$. For a sphere of diameter d , $L_t = L_r = d$, and for a nanorod with a length of l and an aspect ratio of ρ , $L_t = [l / (\ln \rho + C_t)]$ and $L_r = [l / (\sqrt[3]{\ln \rho + C_r})]$. The $L_r^3 \langle \Delta \tilde{u}_r^2 \rangle$ and $L_t \langle \Delta \tilde{r}^2 \rangle$ of our single GNRs in the two PEO solutions is shown with open

and closed symbols, respectively, in Fig. 3(d). As in glycerol, the length of the GNRs in the 6.7% and 12.2% w/w PEO solution samples are determined by aligning the scaled MSDs and MSADs of the GNRs to be $l = 94 \pm 2$ nm in the 6.7% sample and $l = 101 \pm 2$ nm in 12.2%, respectively. Our results compare favorably with $L_t \langle \Delta r^2 \rangle$ of 0.65 μm diameter microspheres, deduced from the previous microrheology study [1] differing systematically by about 15%. Because excess CTAB was added to the PEO solution, we assume that the CTAB layers are intact and that the effective rod diameter, 26 nm, is correspondingly larger than seen using EM.

Small deviations of the GNR data are attributable to two main sources: the aforementioned noise amplification of our mapping procedure at long times and the dynamic error which occurs at short times [53,54], which can be empirically corrected by considering results at different camera exposure times [45]. Physically, our rod motion may deviate from the predictions of the Stokes-Einstein relation due to polymer depletion near the rod surface [5,57] or decoupling from the bulk dynamics of the polymer solution [58–61], but both effects are expected to be small in our system.

As with conventional passive microrheology [1], we used a Fourier representation of the RGSER $G^*(\omega) = [(k_B T)/(\pi s L_r^3 \mathcal{F}\{\langle \Delta \hat{u}_i^2(t) \rangle\})]$ to compute the elastic $G'(\omega)$ and loss $G''(\omega)$ moduli, where $\mathcal{F}\{\langle \Delta \hat{u}_i^2(t) \rangle\}$ is the unilateral Fourier transform of the unbounded MSAD [1]. The elastic and shear moduli of the two PEO solutions obtained from single GNR rotational nanorheology are shown in Figs. 3(e) and 3(f) by open symbols, compared to literature measurements based on diffusive wave spectroscopy [1], shown by lines. In both samples, the maximum frequency at which we can probe the viscoelasticity is limited by the maximum recording speed and the minimum exposure time of the camera, while the minimum frequency is set by the MSAD reaching its asymptote. Notably, considering the size of the measurement uncertainties we have obtained with 100 nm GNRs, the maximum modulus that can be measured by rotational nanorheology, $G_{\text{max}}^* \approx [(K_B T)/(\ell^3 \Delta u_{\text{min}}^2)]$, is 2 orders of magnitude larger than measurable using translational microrheology, $G_{\text{max}}^* \approx [(K_B T)/(l \Delta r_{\text{min}}^2)]$.

The anisotropic translational Brownian motion of the GNR can be characterized by two drag coefficients parallel and perpendicular to its long axis. Following the analysis of Han *et al.* [37], in the moving body frame of the rod, translational displacements, as shown in Fig. 4(a), have a Gaussian distribution, and the corresponding MSDs in a viscous fluid, as plotted in Fig. 4(b), are a linear function of time $\langle \Delta r_{\parallel,\perp}^2 \rangle = 2D_{\parallel,\perp}t$, with D_{\parallel} and D_{\perp} being diffusion coefficients parallel and perpendicular, respectively, to the major axis [Fig. 1(b)]. In a stationary lab frame initially aligned with the rod at $t = 0$, however, rotational diffusion of the GNR erases the particle alignment with the reference frame, causing translational diffusion to become isotropic

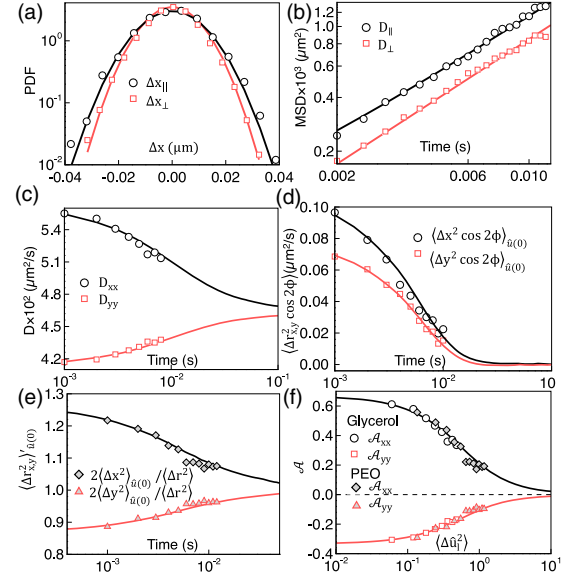


FIG. 4. Anisotropic translational displacement distributions (a), at $\tau = 2$ ms, of a GNR in 90% glycerol (symbols) with a Gaussian fit (lines) and corresponding anisotropic MSDs (b). Diffusion coefficients of the GNR (c), corresponding to the data in (a) and (b), in the fixed lab frame with the x axis aligned with the rod's initial position with the model fit [Eq. (3)]. Mixed translational and orientational correlations (d) in a fixed frame (symbols) and MC simulation (curves). Rescaled anisotropic MSDs (e) of GNR in PEO 6.7% [as in Fig. 3(e)] in the fixed lab frame (symbols) with a viscoelastic model (curves); unscaled MSDs shown in Fig. S14 [45]. Diffusion anisotropy (f), $A_{ii} = (D_{ii} - D_{\perp})/\Delta D$, for a GNR in glycerol and 6.7% PEO solution (symbols), with the model [Eq. (4)] (curves).

[37] for $\tau > \tau_{\theta} = 1/2D_r$. To capture this effect, we decomposed the MSDs of single GNRs into x and y directions with the initial orientation aligned in the x direction, $\langle \Delta r_{x,y}^2 \rangle_{\hat{u}(0)=\hat{e}_x}$; results are shown in Fig. 4(c). As expected initially, $D_{xx}(t < \tau_{\theta})$ equals to D_{\parallel} , and $D_{yy}(t < \tau_{\theta})$ equals to D_{\perp} , before asymptotically approaching $D_t = (D_{\parallel} + 2D_{\perp})/3$ at long times.

To describe such an anisotropic-to-isotropic crossover of the diffusion of uniaxial particles, we generalized the Perrin-Lubensky model [37,38] to three-dimensional rotation [45]. For a rod diffusing in a viscous fluid in 3D, we obtain

$$D_{ii} = \frac{\langle \Delta r_i^2 \rangle_{\hat{u}(0)}}{2t} = D_t + \Delta D \left(u_i^2(0) - \frac{1}{3} \right) \frac{\tau}{t}, \quad (3)$$

where $\Delta D = D_{\parallel} - D_{\perp}$ and $\tau = [1 - \exp(-6D_r t)]/6D_r$, in excellent agreement with the data [Fig. 4(c)]. For an anisotropic particle such as the GNR, the functional dependence of the translational drag coefficients on its orientation mixes correlation between translational and orientational degrees of freedom [37]. For example, we measured two cross terms $\langle \Delta x^2 \cos 2\phi \rangle_{\hat{u}(0)=\hat{e}_x}$ and $\langle \Delta y^2 \cos 2\phi \rangle_{\hat{u}(0)=\hat{e}_x}$,

shown by open symbols in Fig. 4(d), which agree well with the numerical result of MC simulation. We note that this apparent correlation is different from a true cross-coupling of rotational and translational diffusion, which is manifested only with chiral tracers.

Unlike viscous fluids, for viscoelastic materials such as the PEO solution, the mobility tensor of the GNR is a function of both the lag time and the orientation [45], altering the form of the anisotropic-to-isotropic crossover. We extended our model to an arbitrary nonchiral particle in a linear viscoelastic material [45]. As before, we decomposed the MSDs in x and y directions with the initial orientation of $\hat{u}(0) = \hat{e}_x$, for GNRs in viscoelastic PEO solutions [symbols in Fig. 4(e)]. Since the diffusion coefficient is not a constant, we normalized the anisotropic MSDs by their azimuthally averaged values as a function of the lag time. To model these data, we used the creep compliance J of the solution calculated from nanorheology data via $\langle \Delta \hat{u}_l(t)^2 \rangle = 2k_B T L_r^3 J(t)$. While our general model [solid lines in Fig. 4(e)] matches quantitatively with the current measurement, approximations in our approach will fail in the limit of very soft, predominantly elastic materials [45]. Equation (3) and Figs. 4(c) and 4(e) indicate that the rotational diffusion of the GNR controls the rate of the anisotropic-to-isotropic crossover. Therefore, intuitively, one should expect a universal curve for the crossover when plotted against the orientational displacement instead of the time. Figure 4(f) shows such a rescaled diffusion anisotropy defined as $\mathcal{A}_{ii} = (D_{ii} - D_l)/\Delta D$ based on MSAD for the GNR in both glycerol and PEO solutions. The data for both glycerol (open symbols) and PEO (solid symbols) collapse upon each other and the theoretical model

$$\mathcal{A}_{ii} = \left(u_i^2(0) - \frac{1}{3} \right) \frac{1 - \exp(-3\langle \Delta \hat{u}_l(t)^2 \rangle)}{3\langle \Delta \hat{u}_l(t)^2 \rangle}, \quad (4)$$

plotted by solid lines.

Here we have demonstrated that tracking the rotational Brownian motion of nanorods expands the capabilities of passive microrheology to much smaller length scales and stiffer materials. Moreover, particle heating limits allow much stronger laser illumination than we use here, suggesting that smaller GNRs, stiffer materials, and higher frequencies should be accessible. We can imagine mapping out the structure and rheology at the 100 nm scale, resolving a typical bacterium into thousands of subvolumes. The small size of GNRs will also allow the probing of many interfacial systems and soft materials at or near their intrinsic length scales, such as many semiflexible polymer materials at their mesh size or lipid bilayers at the length scale of their thermal undulations. This approach promises access to nanoscale structure, dynamics, and mechanics in a wide variety of biophysical and soft material systems that are currently accessible, if at all, only to state of the art inelastic neutron or dynamics x-ray scattering methods.

This work was supported by Grant No. 55120-NDS from the ACS Petroleum Research Fund, with partial support from the Penn PSOC program, NIH U54-CA193417. We acknowledge useful conversations with Robert Leheny, Eric Weeks, and Tom Lubensky.

*Corresponding author.

jcrocker@seas.upenn.edu

- [1] B. R. Dasgupta, S.-Y. Tee, J. C. Crocker, B. J. Frisken, and D. A. Weitz, Microrheology of polyethylene oxide using diffusing wave spectroscopy and single scattering, *Phys. Rev. E* **65**, 051505 (2002).
- [2] T. G. Mason, Estimating the viscoelastic moduli of complex fluids using the generalized Stokes–Einstein equation, *Rheol. Acta* **39**, 371 (2000).
- [3] T. G. Mason, K. Ganesan, J. H. Van Zanten, D. Wirtz, and S. C. Kuo, Particle Tracking Microrheology of Complex Fluids, *Phys. Rev. Lett.* **79**, 3282 (1997).
- [4] T. G. Mason and D. A. Weitz, Optical Measurements of Frequency-Dependent Linear Viscoelastic Moduli of Complex Fluids, *Phys. Rev. Lett.* **74**, 1250 (1995).
- [5] D. T. Chen, E. R. Weeks, J. C. Crocker, M. F. Islam, R. Verma, J. Gruber, A. J. Levine, T. C. Lubensky, and A. G. Yodh, Rheological Microscopy: Local Mechanical Properties from Microrheology, *Phys. Rev. Lett.* **90**, 108301 (2003).
- [6] J. C. Crocker, M. T. Valentine, E. R. Weeks, T. Gisler, P. D. Kaplan, A. G. Yodh, and D. A. Weitz, Two-point microrheology of inhomogeneous soft materials, *Phys. Rev. Lett.* **85**, 888 (2000).
- [7] M. L. Gardel, M. T. Valentine, J. C. Crocker, A. R. Bausch, and D. A. Weitz, Microrheology of Entangled F -actin Solutions, *Phys. Rev. Lett.* **91**, 158302 (2003).
- [8] A. W. C. Lau, B. D. Hoffman, A. Davies, J. C. Crocker, and T. C. Lubensky, Microrheology, Stress Fluctuations, and Active Behavior of Living Cells, *Phys. Rev. Lett.* **91**, 198101 (2003).
- [9] K. He, F. Babaye Khorasani, S. T. Retterer, D. K. Thomas, J. C. Conrad, and R. Krishnamoorti, Diffusive Dynamics of Nanoparticles in Arrays of Nanoposts, *ACS Nano* **7**, 5122 (2013).
- [10] T. M. Squires and T. G. Mason, Fluid mechanics of microrheology, *Annu. Rev. Fluid Mech.* **42**, 413 (2010).
- [11] Z. Cheng and T. G. Mason, Rotational Diffusion Microrheology, *Phys. Rev. Lett.* **90**, 018304 (2003).
- [12] E. Andablo-Reyes, P. Díaz-Leyva, and J. L. Arauz-Lara, Microrheology from Rotational Diffusion of Colloidal Particles, *Phys. Rev. Lett.* **94**, 106001 (2005).
- [13] C. Haro-Pérez, E. Andablo-Reyes, P. Díaz-Leyva, and J. L. Arauz-Lara, Microrheology of viscoelastic fluids containing light-scattering inclusions, *Phys. Rev. E* **75**, 041505 (2007).
- [14] F. C. Cheong and D. G. Grier, Rotational and translational diffusion of copper oxide nanorods measured with holographic video microscopy, *Opt. Express* **18**, 6555 (2010).
- [15] K. V. Edmond, M. T. Elssesser, G. L. Hunter, D. J. Pine, and E. R. Weeks, Decoupling of rotational and translational diffusion in supercooled colloidal fluids, *Proc. Natl. Acad. Sci. U.S.A.* **109**, 17891 (2012).

- [16] G. L. Hunter, K. V. Edmond, M. T. Elseser, and E. R. Weeks, Tracking rotational diffusion of colloidal clusters, *Opt. Express* **19**, 17189 (2011).
- [17] D. Mukhija and M. J. Solomon, Translational and rotational dynamics of colloidal rods by direct visualization with confocal microscopy, *J. Colloid Interface Sci.* **314**, 98 (2007).
- [18] A. Wang, T. G. Dimiduk, J. Fung, S. Razavi, I. Kretschmar, K. Chaudhary, and V. N. Manoharan, Using the discrete dipole approximation and holographic microscopy to measure rotational dynamics of non-spherical colloidal particles, *J. Quant. Spectrosc. Radiat. Transfer* **146**, 499 (2014).
- [19] X. Cheng, X. Cao, B. Xiong, Y. He, and E. S. Yeung, Background-free three-dimensional selective imaging of anisotropic plasmonic nanoparticles, *Nano Res.* **10**, 1423 (2017).
- [20] K. Marchuk and N. Fang, Three-dimensional orientation determination of stationary anisotropic nanoparticles with sub-degree precision under total internal reflection scattering microscopy, *Nano Lett.* **13**, 5414 (2013).
- [21] K. Marchuk, J. W. Ha, and N. Fang, Three-dimensional high-resolution rotational tracking with superlocalization reveals conformations of surface-bound anisotropic nanoparticles, *Nano Lett.* **13**, 1245 (2013).
- [22] C. Sönnichsen and A. P. Alivisatos, Gold nanorods as novel nonbleaching plasmon-based orientation sensors for polarized single-particle microscopy, *Nano Lett.* **5**, 301 (2005).
- [23] E. J. Titus and K. A. Willets, Accuracy of superlocalization imaging using gaussian and dipole emission point-spread functions for modeling gold nanorod luminescence, *ACS Nano* **7**, 6258 (2013).
- [24] G. Wang, W. Sun, Y. Luo, and N. Fang, Resolving rotational motions of nano-objects in engineered environments and live cells with gold nanorods and differential interference contrast microscopy, *J. Am. Chem. Soc.* **132**, 16417 (2010).
- [25] A. J. Wilson and K. A. Willets, Surface-enhanced Raman scattering imaging using noble metal nanoparticles, *Wiley Interdiscip. Rev.: Nanomed. Nanobiotechnol.* **5**, 180 (2013).
- [26] L. Xiao, Y. Qiao, Y. He, and E. S. Yeung, Three dimensional orientational imaging of nanoparticles with darkfield microscopy, *Anal. Chem.* **82**, 5268 (2010).
- [27] L. Xiao, Y. Qiao, Y. He, and E. S. Yeung, Imaging translational and rotational diffusion of single anisotropic nanoparticles with planar illumination microscopy, *J. Am. Chem. Soc.* **133**, 10638 (2011).
- [28] L. Xiao, L. Wei, C. Liu, Y. He, and E. S. Yeung, Un-synchronized translational and rotational diffusion of nanocargo on a living cell membrane, *Angew. Chem., Int. Ed.* **51**, 4181 (2012).
- [29] L. Xiao and E. S. Yeung, Optical imaging of individual plasmonic nanoparticles in biological samples, *Annu. Rev. Anal. Chem.* **7**, 89 (2014).
- [30] D. Xu, Y. He, and E. S. Yeung, Direct imaging of transmembrane dynamics of single nanoparticles with darkfield microscopy: improved orientation tracking at cell sidewall, *Anal. Chem.* **86**, 3397 (2014).
- [31] H. Yuan, S. Khatua, P. Zijlstra, and M. Orrit, Individual gold nanorods report on dynamical heterogeneity in supercooled glycerol, *Faraday Discuss.* **167**, 515 (2013).
- [32] S. Alam and A. Mukhopadhyay, Translational and rotational diffusions of nanorods within semidilute and entangled polymer solutions, *Macromolecules* **47**, 6919 (2014).
- [33] S. Alam and A. Mukhopadhyay, Translational anisotropy and rotational diffusion of gold nanorods in colloidal sphere solutions, *Langmuir* **31**, 8780 (2015).
- [34] R. K. Chhetri, R. L. Blackmon, W.-C. Wu, D. B. Hill, B. Button, P. Casbas-Hernandez, M. A. Troester, J. B. Tracy, and A. L. Oldenburg, Probing biological nanotopology via diffusion of weakly constrained plasmonic nanorods with optical coherence tomography, *Proc. Natl. Acad. Sci. U.S.A.* **111**, E4289 (2014).
- [35] R. K. Chhetri, K. A. Kozek, A. C. Johnston-Peck, J. B. Tracy, and A. L. Oldenburg, Imaging three-dimensional rotational diffusion of plasmon resonant gold nanorods using polarization-sensitive optical coherence tomography, *Phys. Rev. E* **83**, 040903 (2011).
- [36] R. K. Chhetri and A. L. Oldenburg, in *Frontiers in Optics* (Optical Society of America, Washington, DC, 2012), p. FTu4E. 3.
- [37] Y. Han, A. M. Alsayed, M. Nobili, J. Zhang, T. C. Lubensky, and A. G. Yodh, Brownian motion of an ellipsoid, *Science* **314**, 626 (2006).
- [38] F. Perrin, Mouvement Brownien d'un ellipsoïde (II). Rotation libre et dépolarisation des fluorescences. Translation et diffusion de molécules ellipsoïdales, *J. Phys. Radium* **7**, 1 (1936).
- [39] S. Link and M. A. El-Sayed, Spectral properties and relaxation dynamics of surface plasmon electronic oscillations in gold and silver nanodots and nanorods, *J. Phys. Chem. B* **103**, 8410 (1999).
- [40] C. F. Bohren and D. R. Huffman, *Absorption and Scattering of Light by Small Particles* (John Wiley & Sons, New York, 1983), p. 82.
- [41] A. Brioude, X. Jiang, and M. Pileni, Optical properties of gold nanorods: DDA simulations supported by experiments, *J. Phys. Chem. B* **109**, 13138 (2005).
- [42] P. K. Jain, S. Eustis, and M. A. El-Sayed, Plasmon coupling in nanorod assemblies: optical absorption, discrete dipole approximation simulation, and exciton-coupling model, *J. Phys. Chem. B* **110**, 18243 (2006).
- [43] E. M. Purcell and C. R. Pennypacker, Scattering and absorption of light by nonspherical dielectric grains, *Astrophys. J.* **186**, 705 (1973).
- [44] M. A. Yurkin and A. G. Hoekstra, The discrete-dipole-approximation code ADDA: capabilities and known limitations, *J. Quant. Spectrosc. Radiat. Transfer* **112**, 2234 (2011).
- [45] See Supplemental Material at <http://link.aps.org/supplemental/10.1103/PhysRevLett.120.118002> for additional details about the experimental setup, sample preparation, simulations, and derivation, which includes Refs. [46–52].
- [46] D. Axelrod, Carbocyanine dye orientation in red cell membrane studied by microscopic fluorescence polarization, *Biophys. J.* **26**, 557 (1979).
- [47] H. J. Chen, L. Shao, Q. Li, and J. F. Wang, Gold nanorods and their plasmonic properties, *Chem. Soc. Rev.* **42**, 2679 (2013).
- [48] P. B. Johnson and R. W. Christy, Optical constants of the noble metals, *Phys. Rev. B* **6**, 4370 (1972).

- [49] M. Khan and T. G. Mason, Trajectories of probe spheres in generalized linear viscoelastic complex fluids, *Soft Matter* **10**, 9073 (2014).
- [50] M. Khan and T. G. Mason, Random walks of colloidal probes in viscoelastic materials, *Phys. Rev. E* **89**, 042309 (2014).
- [51] I. Teraoka, *Front Matter and Index* (Wiley Online Library, New York, 2002).
- [52] M. Rubinstein and R. H. Colby, *Polymer Physics* (Oxford University, New York, 2003), Vol. 23.
- [53] J. C. Crocker and D. G. Grier, Methods of digital video microscopy for colloidal studies, *J. Colloid Interface Sci.* **179**, 298 (1996).
- [54] T. Savin and P. S. Doyle, Static and dynamic errors in particle tracking microrheology, *Biophys. J.* **88**, 623 (2005).
- [55] I. Martchenko, H. Dietsch, C. Moitzi, and P. Schurtenberger, Hydrodynamic properties of magnetic nanoparticles with tunable shape anisotropy: prediction and experimental verification, *J. Phys. Chem. B* **115**, 14838 (2011).
- [56] M. M. Tirado, C. L. Martínez, and J. G. de la Torre, Comparison of theories for the translational and rotational diffusion coefficients of rod-like macromolecules. Application to short DNA fragments, *J. Chem. Phys.* **81**, 2047 (1984).
- [57] A. J. Levine and T. C. Lubensky, One- and Two-Particle Microrheology, *Phys. Rev. Lett.* **85**, 1774 (2000).
- [58] L.-H. Cai, S. Panyukov, and M. Rubinstein, Mobility of nonsticky nanoparticles in polymer liquids, *Macromolecules* **44**, 7853 (2011).
- [59] Y. Cheng, R. K. Prud'Homme, and J. L. Thomas, Diffusion of mesoscopic probes in aqueous polymer solutions measured by fluorescence recovery after photobleaching, *Macromolecules* **35**, 8111 (2002).
- [60] I. Kohli and A. Mukhopadhyay, Diffusion of nanoparticles in semidilute polymer solutions: effect of different length scales, *Macromolecules* **45**, 6143 (2012).
- [61] R. Poling-Skutvik, R. Krishnamoorti, and J. C. Conrad, Size-dependent dynamics of nanoparticles in unentangled polyelectrolyte solutions, *ACS Macro Lett.* **4**, 1169 (2015).

Supporting Information for

Nanoscale Rheology via Single Gold Nanorod Rotational Diffusion

*Mehdi Molaie, Ehsan Atefi, John C. Crocker**

Chemical and Biomolecular Engineering, University of Pennsylvania,

220 S. 33rd St, Philadelphia, PA 19104

1. Discrete Dipole Approximation (DDA)

Far-field scattered light of a single GNR can be modeled by the electric field emitted from three independent and orthogonal dipoles. To determine the oscillator strength of each dipole we used DDA [1,2]. We modeled the GNR as a spherocylinder, as shown in Figure S1, with refractive index n_g [3], diameter d and length b , and hemisphere radius $d/2$. We discretized the GNR using at least 1000 dipoles per wavelength with uniform lattice distance between dipoles. To determine the oscillator strength of the longitudinal and transverse dipoles we ran DDA with GNR major axis respectively parallel and normal to the electric field of the incident beam. We also ran DDA to model a rod with flat ends and an ellipsoidal particle. Figure S1 shows the three models discretized into arrays of voxels. Table S1 shows the DDA results for three models. To validate that DDA yields reliable results with our voxelation, we compared the DDA results for an ellipsoid to the analytic Gans theory, [4] showing excellent agreement.

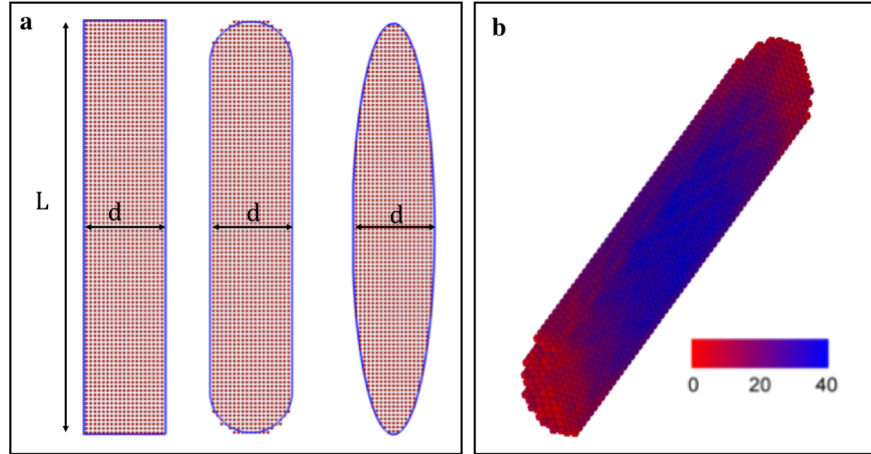


Figure S1: a) Voxellations of the three different particles. The simulation is performed on particles with $L=100\text{nm}$ and $d=20\text{ nm}$. b) Discrete dipoles in a spherocylinder color coded with their oscillator strength when the incident electric field is parallel to the major axis of the rod.

Table S1: The polarizability of the longitudinal and transverse dipoles representing a spherocylinder, flat cylinder, and ellipsoidal particle normalized by the volume of the particles in two different wave lengths. The bottom row is the result obtained using Gans theory [4] which shows good agreement with DDA result.

		$\lambda = 532\text{ nm}$			$\lambda = 670\text{ nm}$		
		α_l/V	α_t/V	γ	α_l/V	α_t/V	γ
DDA	Spherocylinder	0.5	0.26	2.0	6.8	0.2	33
	Flat cylinder	0.5	0.25	2.0	8.2	0.2	40.32
	Ellipsoid	0.6	0.25	2.4	4.6	0.2	23
Theory[4]		0.61	0.24	2.4	4.7	0.2	23.5

2. Laser-illuminated Dark field Microscope.

Dark-field microscopy, which blocks the illumination beam (and its reflections) has been used to image nanoparticles and their motion for more than a century. Coupled with laser-illumination, it allows sufficient signal to be produced in a short exposure, allowing high-speed precision tracking. Our custom build instrument focuses a single mode diode pumped solid state laser in the back-aperture of a high-NA, immersion objective to produce a small (diameter FWHM = $28\ \mu\text{m}$), collimated Gaussian beam in the specimen, see Figure S2a. This laser is relayed to the objective using a window with a small spot of reflective silver deposited on the optical axis, which allows most of the imaging light returning from the

specimen to pass to the imaging system. Unscattered illumination light exits the specimen vertically, while light reflected from the planar interfaces of the sample chamber is reflected back towards the laser by the spot, yielding a dark background field. Relay optics outside the microscope body produce a secondary infinity space where a larger paraxial mask and Wollaston prism are located to separate the light's orthogonal polarizations, and project them onto a high-speed camera with a CMOS detector.

Figure S2b shows the optical path of the dark field microscopy. The light source is a single longitudinal mode diode pumped solid state (DPSS) laser (Shanghai dream laser SDL-671-300T) delivering linearly polarized light with wave length of 670 nm with beam size of 0.75 mm and power of 300mW. The light passes through a quarter wave plate (Thorlab WPMQ05M-670) to generate a circularly polarized beam. A beam expander constructed from two doublet lenses with $f=-20$ mm and $f=125$ mm (Thorlabs) magnifies the beam size to 5.6mm. The laser beam is then focused on the back aperture of the objective with a $f=40$ cm doublet lens after having been reflected by the dot mirror. The reflecting surface of the dot mirror was formed by sputter coating of silver and TiO₂ on its central region. The TiO₂ layer protects the silver mirror from oxidation. The mirror has an elliptical shape with minor axis of 2.5 mm and the major axis of 3.53 mm.

The scattered light from GNRs is collected by an oil immersion objective (Leica HCX PL APO 100X-1.4) and sent to an external relay system constructed by two doublet lenses with $f=150$ cm and $f=300$ cm which deliver 2x image magnification. In the infinity space between these two lenses, the scattered light passes around an additional paraxial mask constructed with a 3/32" bearing ball (McMaster Carr 9642K25) attached to a glass slide and positioned in the conjugate plane and then passes through a Wollaston prism (Thorlab WPQ10), that separates the light into two orthogonally polarized beams with a 1° separation angle. The two beams focus to the same axial but different lateral positions. The lateral displacement of the two beams from each other, d , was set by the separation angle, θ , and focal length of the lens, f , is $d=f\theta$. In the current optical path $d=5.2$ mm which is half of the size of the CMOS sensor.

An adjustable slit (Thorlab VA100) is located in the first image plane to prevent any superposition of the two images on the detector. The images of GNRs were recorded by CMOS

Phantom IV camera (Vision Research) at different frame rates. The effective pixel scale in the specimen plane of the microscope is $0.100 \pm 0.003 \mu\text{m}$.

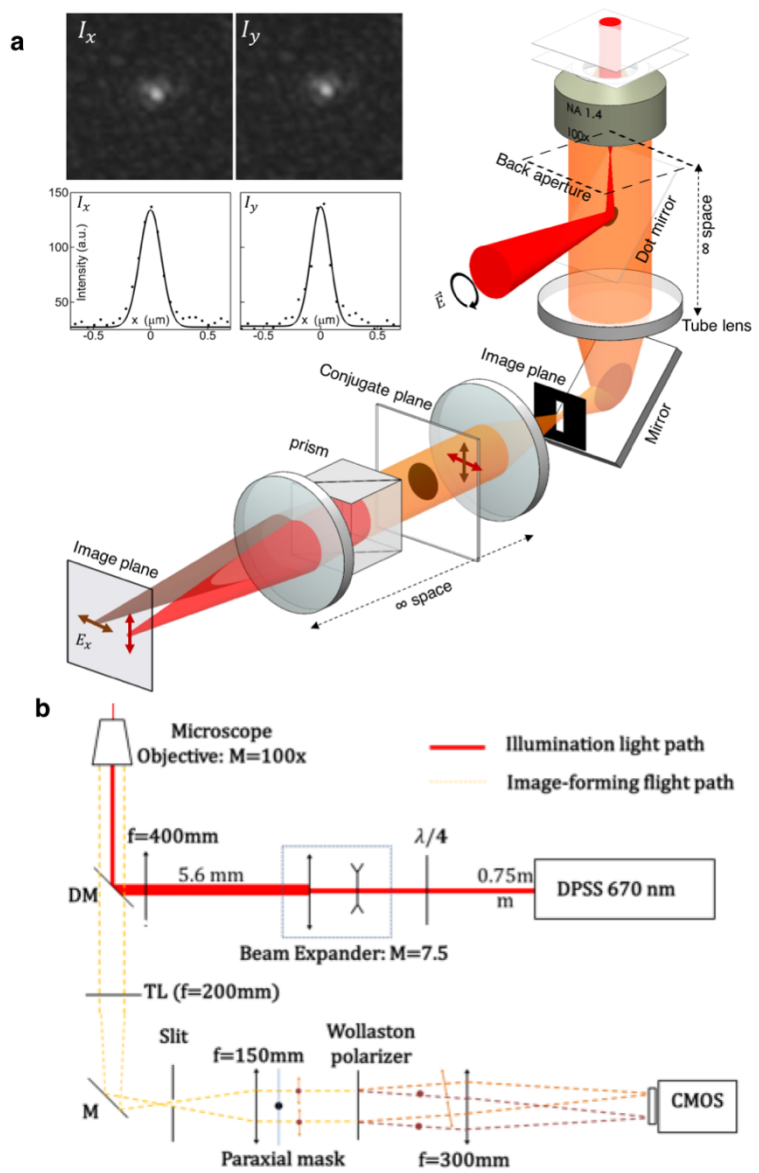


Figure S2: Schematic optical path of the dark field microscopy with orthogonally polarized imaging system.

The location of the GNR were tracked using a MATLAB particle tracking algorithm [5]. Custom MATLAB codes were used to convert the intensity of the GNRs to orientations and compute the MSD and MSAD. This system is qualified using a test sample of 100 nm polystyrene nanospheres; see Figure S2a inset. The symmetry between the two orthogonally

polarized images confirms the circular polarization of our illumination, polarization preservation in our imaging system and the azimuthal symmetry of the nanospheres. The Airy disk is consistent with expectations for our high-NA imaging system with a large paraxial mask, having a slightly smaller core (FWHM = 225 nm) and more pronounced diffraction rings than an unmasked system.

3. Sample preparation

The CTAB coated gold nanorod solution was purchased from Nanopartz (A12-20-900-CTAB-DIH-25) with a GNR concentration of 4.9×10^{11} particles/ml and CTAB concentration of 3mM. To embed the GNRs in glycerol, 0.1 ml of the GNR solution was centrifuged, and the supernatant was replaced by 1 ml Glycerol. The sample were gently stirred for two days to obtain a uniform distribution of the GNR in glycerol. The size distribution of GNRs used in the experiments is show in figure S3.

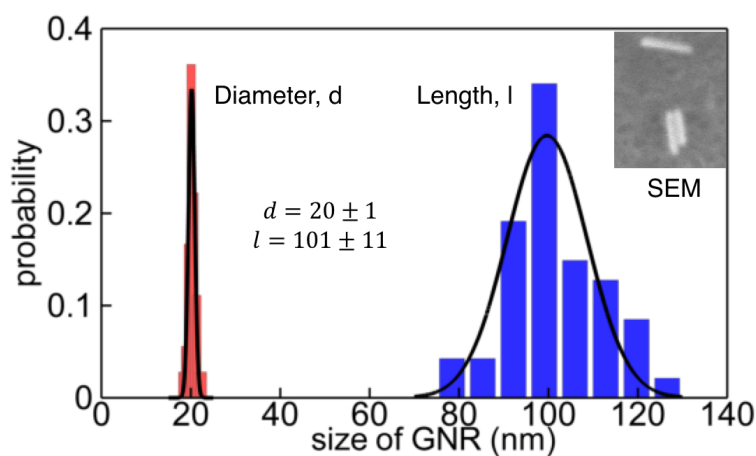


Figure S3: The probability distribution of the diameter and length of the GNR Obtained from SEM images.

Inset: A sample of SEM of the GNR

Two solutions of polymer with concentrations of 7.4 wt% and 13.4 wt% were prepared by mixing polyethylene oxide with average molecular weight of 200K (181994 Sigma Aldrich) in 5mM CTAB solution in deionized water to stabilize the CTAB layer on the GNRs. The solutions were shaken gently for 2 days to achieve homogenous PEO solution. The 0.1 ml of GNR solution were then added to 0.9 ml of each solution. The final PEO concentrations of samples were 6.7 wt% and 12.2 wt%, and the concentrations of GNR in both samples are ~ 0.1

nM. We continued to gently shake the samples with embedded GNR for three more days to uniformly distribute GNRs in the PEO samples.

4. Detail of polarimetry analysis

Our first task is to analytically derive the intensity of scattered light at the imaging detector of our microscope, in two orthogonally polarized channels, due to scattering by the three principal dipoles of the GNR. The model includes the effect of large NA objective and the paraxial mask forming the imaging system. The orientation of the GNR can be defined by polar, β , and azimuthal angle, ϕ , as shown in Figure S3a,b. Here we describe the detailed model of scattering intensity from three orthogonally oscillating dipoles collected by the dark field microscope in two orthogonally polarized channels.

In general, the scattering intensity from each dipole is proportional to the square of oscillator strength and the collection probability function of the imaging system, $I_{x,y}^j = S^j P_{x,y}$ where $j=1$ denotes the longitudinal dipoles and $j=2,3$ denote two transverse dipoles; x and y denote each polarized channel. The oscillator strength of each dipole depends on the cross product of the orientation of dipole, \hat{s}^j respect to the external electric field; therefore, we first simply determined the angles of each dipole based on the polar and azimuthal angles of the GNR β , and ϕ , Figure S4.

$$\beta_1 = \beta, \phi_1 = \phi \rightarrow \hat{s}^1 = \sin \beta \cos \phi \hat{e}_x + \sin \beta \sin \phi \hat{e}_y + \cos \beta \hat{e}_z, \quad (S1a)$$

$$\beta_2 = \beta + \frac{\pi}{2}, \phi_2 = \phi \rightarrow \hat{s}^2 = -\cos \beta \cos \phi \hat{e}_x - \cos \beta \sin \phi \hat{e}_y + \sin \beta \hat{e}_z, \quad (S1b)$$

$$\beta_3 = \frac{\pi}{2}, \phi_3 = \phi + \frac{\pi}{2} \rightarrow \hat{s}^3 = \sin \phi \hat{e}_x - \cos \phi \hat{e}_y. \quad (S1c)$$

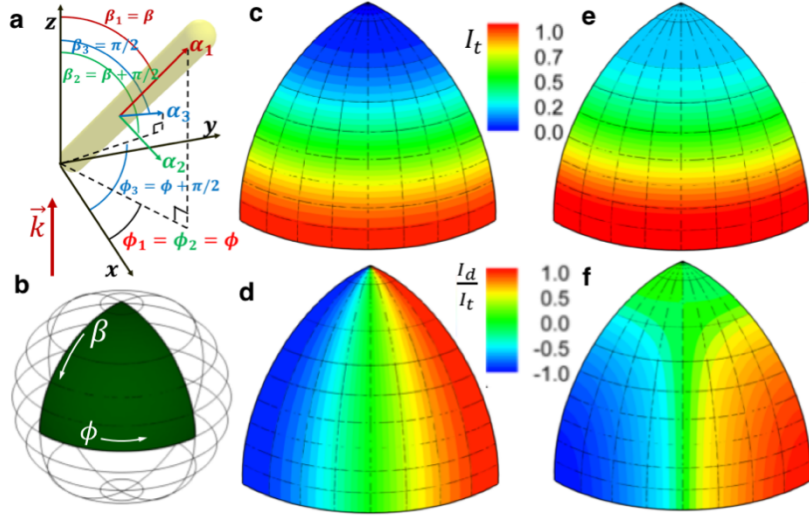


Figure S4: (a-b) Coordinate system of the GNR defined by polar, β , and azimuthal angles, ϕ . (c & e) 3-d map of the total intensity of the scattered light and (d & f) the intensity difference between two orthogonal channels at different orientation of the GNR. (c-d) Expected signal from a single dipole, collected with a low-NA objective. (e-f) Scattered light from a GNR with three orthogonal dipoles collected with a high NA objective.

In our inverted, epi-illuminated dark field microscope, the external electric field is circularly polarized plane wave beam along optical axis, $\hat{e} = \hat{e}_x + \hat{e}_y$. The strength of each dipole is $S^j = (\alpha^j \hat{s}^j \hat{e}_z)^2$ which leads to:

$$S^1 \propto \alpha_1^2 \sin^2 \beta, \quad (S2a)$$

$$S^2 \propto \alpha_2^2 \cos^2 \beta, \quad (S2b)$$

$$S^3 \propto \alpha_3^2. \quad (S2c)$$

The collection probability function of each dipole is determined based on their orientation:

$$P_x^1 = c_1 \sin^2 \beta \cos^2 \phi + c_2 \sin^2 \beta \sin^2 \phi + c_3 \cos^2 \beta, \quad (S3a)$$

$$P_y^1 = c_1 \sin^2 \beta \sin^2 \phi + c_2 \sin^2 \beta \cos^2 \phi + c_3 \cos^2 \beta, \quad (S3a)$$

$$P_x^2 = c_1 \cos^2 \beta \cos^2 \phi + c_2 \cos^2 \beta \sin^2 \phi + c_3 \sin^2 \beta, \quad (S3b)$$

$$P_y^2 = c_1 \cos^2 \beta \sin^2 \phi + c_2 \cos^2 \beta \cos^2 \phi + c_3 \sin^2 \beta, \quad (S3b)$$

$$P_x^3 = c_1 \cos^2 \phi + c_2 \sin^2 \phi, \quad (S3c)$$

$$P_y^3 = c_1 \sin^2 \phi + c_2 \cos^2 \phi. \quad (S3c)$$

Finally, the scattering intensity in each channel is determined as:

$$I_x = S^1 P_x^1 + S^2 P_x^2 + S^3 P_x^3 = c_1[\alpha_t^2 \sin^4 \beta \cos^2 \phi + \alpha_t^2(\sin^2 \phi + \cos^4 \beta \cos^2 \phi)] + c_2[\alpha_t^2 \sin^4 \beta \sin^2 \phi + \alpha_t^2(\cos^2 \phi + \cos^4 \beta \sin^2 \phi)] + c_3[\alpha_t^2 \sin^2 \beta \cos^2 \beta + \alpha_t^2(\cos^2 \beta \sin^2 \beta \cos^2 \phi)], \quad (S4a)$$

$$I_y = S^1 P_y^1 + S^2 P_y^2 + S^3 P_y^3 = c_1[\alpha_t^2 \sin^4 \beta \sin^2 \phi + \alpha_t^2(\cos^2 \phi + \cos^4 \beta \sin^2 \phi)] + c_2[\alpha_t^2 \sin^4 \beta \cos^2 \phi + \alpha_t^2(\sin^2 \phi + \cos^4 \beta \cos^2 \phi)] + c_3[\alpha_t^2 \sin^2 \beta \cos^2 \beta + \alpha_t^2(\cos^2 \beta \sin^2 \beta \sin^2 \phi)], \quad (S4b)$$

where c_1 , c_2 , and c_3 are correction factors of the dark field imaging system accounting for the cone angles corresponding to the numerical aperture of high NA of objective and the diameter of paraxial stop in the optical path. In the case of imaging with no paraxial mask, the collection factors are determined by [6]:

$$c_1(\delta) = \frac{1}{8} [5 - 3 \cos \delta - \cos^2 \delta - \cos^3 \delta] / [1 - \cos \delta], \quad (S5a)$$

$$c_2(\delta) = \frac{1}{24} [1 - 3 \cos \delta + 3 \cos^2 \delta - \cos^3 \delta] / [1 - \cos \delta], \quad (S5b)$$

$$c_3(\delta) = \frac{1}{6} [2 - 3 \cos \delta + \cos^3 \delta] / [1 - \cos \delta], \quad (S5c)$$

where $\delta = \delta_{max} = \sin^{-1}(NA/n)$ is the maximum half-angle of the collection cone. For an objective with NA=1.4 and n=1.53 and no paraxial mask, c_1 , c_2 , and c_3 are estimated to be 0.75, 0.01, and 0.24. The values show the large aperture limit since c_1 is not the only main correction factor. The presence of the paraxial mask in the optical path cuts off the center of the scattered light beam and modifies the collection properties of the imaging system. The angle of the collection cone, therefore, is between δ_{max} and nonzero minimum angle δ_{min} which depends on the size of the paraxial mask $\delta_{min} = \tan^{-1}\left(\frac{r_{mask}}{f_{obj}}\right)$, where r_{mask} and f_{obj} are the radius of the paraxial mask and the focal length of the objective respectively. The collection factors in this case are

$$c_1 = c_1(\delta_{max}) - c_1(\delta_{min}), \quad (S6a)$$

$$c_2 = c_2(\delta_{max}) - c_2(\delta_{min}), \quad (S6b)$$

$$c_3 = c_3(\delta_{max}) - c_3(\delta_{min}). \quad (S6c)$$

The intensity of scattered light in each channel can be formulated as following:

$$I_x = c_1[\sin^4 \beta \cos^2 \phi + \gamma^2(\sin^2 \phi + \cos^4 \beta \cos^2 \phi)] + c_2[\sin^4 \beta \sin^2 \phi + \gamma^2(\cos^2 \phi + \cos^4 \beta \sin^2 \phi)] + c_3[\sin^2 \beta \cos^2 \beta + \gamma^2(\cos^2 \beta \sin^2 \beta \cos^2 \phi)], \quad (S7a)$$

$$I_y = c_1[\sin^4 \beta \sin^2 \phi + \gamma^2(\cos^2 \phi + \cos^4 \beta \sin^2 \phi)] + c_2[\sin^4 \beta \cos^2 \phi + \gamma^2(\sin^2 \phi + \cos^4 \beta \cos^2 \phi)] + c_3[\sin^2 \beta \cos^2 \beta + \gamma^2(\cos^2 \beta \sin^2 \beta \sin^2 \phi)]. \quad (\text{S7b})$$

Our second task is to invert the functional dependence of the two polarized intensities on the GNR orientation, to compute the orientation from the two measured intensities. Intuitively, we find that polar angle depends on the sum of the two intensities, independent of the azimuthal angle, while the azimuthal angle can be computed from the difference in the two intensities. The expression for the total intensity, I_t , of scattered light simplifies to

$$I_t = C_t[(1 - N)\sin^4 \beta + (N - \Gamma)\sin^2 \beta + \Gamma], \quad (\text{S8})$$

where $N = \frac{c_3}{c_1}$ and $\Gamma = \frac{2\gamma^2}{1+\gamma^2}$ are properties of the imaging system and the effect of the transverse dipoles, respectively, and C_t is a constant factor depending on the overall scattering cross-section and detector efficiency. Notably, the total intensity only depends on the polar angle, β . Figure S4c and e shows the dependency of the total intensity on the orientation of the GNR in two different cases. Figure S4c depicts the case when the polarizability of the transverse dipoles is negligible, $\Gamma = 0$; hence, the total recorded intensity is zero when the nanorod is normal to the image plane, $\beta = 0$. However, as shown in Figure S4e, when $\Gamma \neq 0$ the total intensity is always larger than zero. Similarly, the difference between two polarized intensities, I_d , (equations S7a,b) is given by

$$I_d \approx C_d \cos 2\phi \sin^2 \beta [\sin^2 \beta - \Gamma + N\Gamma(1 - \sin^2 \beta)]. \quad (\text{S9})$$

Intuitively, the intensity difference between two orthogonal channels in the case of paraxial (small NA) imaging and a single dipole, $\Gamma = 0$, $N = 0$, only depends on the azimuthal angle; ϕ can be computed from: $\cos 2\phi = I_d/I_t$, see Figure S4d. While in the general case in Eq. S9 the intensity difference depends on both azimuthal and polar angles, see Figure 1f, the azimuthal angle can still be readily determined since the polar angle can be determined separately from the total intensity. As might be expected, the two intensities in Eq. S7 are periodic and symmetric in the azimuthal and polar angles, respectively. When inverting to solve for the polar angle there are two possible solutions, for the azimuthal angle there are four possible values. In general, the particle orientation is mapped onto a single octant of the unit sphere, depicted in Figure S4b. While this is limiting when trying to determine the absolute spatial orientation of the rod, for determining the angular mean-squared displacement for performing microrheology, it provides little impediment. Notably, it appears

possible to remove this ambiguity by fitting the Airy disk of the out of focus image, but we do not examine this possibility here.

5. Rotational and translational diffusion of single GNRs in Glycerol

At lag time $\tau = 0.3s \approx 2\tau_\theta$, where $\tau_\theta = 1/2D_r$ is the GNR tumbling time, the distribution of the translational displacements, marked by open circles in Figure S5d, is Gaussian, as expected. The expected distribution of bounded rotational displacements at short lag times, over a sphere or octant, follows a Rayleigh distribution instead of being Gaussian, see Figure S4d, similar to Monte Carlo simulation. Rotational displacements in glycerol, Figure S5e, show that $P(|\Delta\hat{u}|)$ indeed follow a Rayleigh distribution.

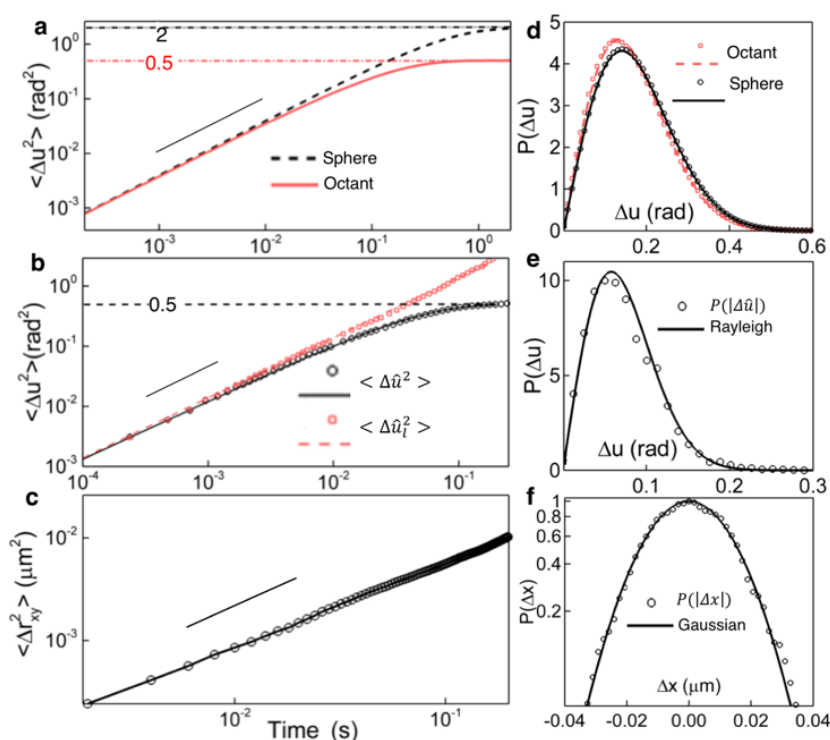


Figure S5 (a) Simulated MSAD of the GNR randomly reorienting over a unit sphere (dashed black line) and MSAD of the same GNR with orientation mapped over a unit octant (solid red line). Horizontal lines indicate the expected asymptote for MSADs. (b) Measured MSAD of the GNR embedded in glycerol (circles) and mapped unbounded MSAD (squares). Stretched exponential fit (solid line) on measured MSAD and linear fit on mapped unbounded MSAD (dashed line) leads to identical rotational diffusional coefficient. (c) MSD of the GNR in glycerol. (d) Modeled probability distribution of bounded rotational displacement over a sphere (circles) and octant (squares) by Monte Carlo simulation follow Rayleigh distribution (lines). (e) Measured probability distribution of rotational displacement of the GNR in glycerol at lag time $\tau = 0.01s$ (circles) and fitted Rayleigh distribution (line). Measured probability distribution of the translational displacement (circles) at lag time $\tau = 0.3s$ shows Gaussian distribution (line).

6. Random walk over sphere

To simulate the orientational random walk trajectory of the rod, $\hat{s}(t)$, we generated a 2D translational random walk of a Brownian bead over a unit sphere which replicates motion of the tip of the rod respect to its center of mass. The basic idea is that at each time step the bead randomly walks on a plane tangent to the unit sphere. Therefore, as the particle moves, the plane also moves and reorients on the unit sphere. We first generated two sets of Gaussian-distributed random number $\{\Delta x, \Delta y\}$, each containing N elements. Each set has a mean of zero and a standard deviation of $4D_r^2\Delta t^2$, where D_r is the rotational diffusion coefficient of Brownian motion, and Δt is the time step size.

If at time $t = n\Delta t$, $\hat{r}(t) = [x_s(t), y_s(t), z_s(t)]$ indicates the position of the particles on the sphere, the next step of the random walk happens on the plane normal to the \hat{r} . At each time step, we also generate a random set of two orthogonal unit vectors $\{\hat{u}_1, \hat{u}_2\}$ on the plane. These vectors determine the direction of the random walk. To construct these vectors, we first generate a random vector, \hat{u}_r with three random numbers with Normal distribution. The generated vector is normalized by its size. Then, $\{\hat{u}_1, \hat{u}_2\}$ are generated as follows:

$$\hat{u}_1 = \frac{\hat{r}(t) \times \hat{u}_r}{|\hat{r}(t) \times \hat{u}_r|}, \quad (\text{S10a})$$

$$\hat{u}_2 = \frac{\hat{r}(t) \times \hat{u}_1}{|\hat{r}(t) \times \hat{u}_1|}. \quad (\text{S10b})$$

The next position of the bead is then determined as:

$$\hat{r}(t + \Delta t) = \frac{\hat{r}(t) + \Delta x_{n+1} \hat{u}_1 + \Delta y_{n+1} \hat{u}_2}{|\hat{r}(t) + \Delta x_{n+1} \hat{u}_1 + \Delta y_{n+1} \hat{u}_2|}. \quad (\text{S11})$$

We produce an orientational trajectory of a nanorod with rotational diffusion of $D_r = 1 \text{ rad}^2/\text{s}$ and $\Delta t = 0.1 \text{ ms}$. The result trajectory is shown in Figure S6a. To project the trajectory to the octant, we simply use the absolute values of the components of the orientational vector. The projected trajectory on the octant is shown in Figure S6b.

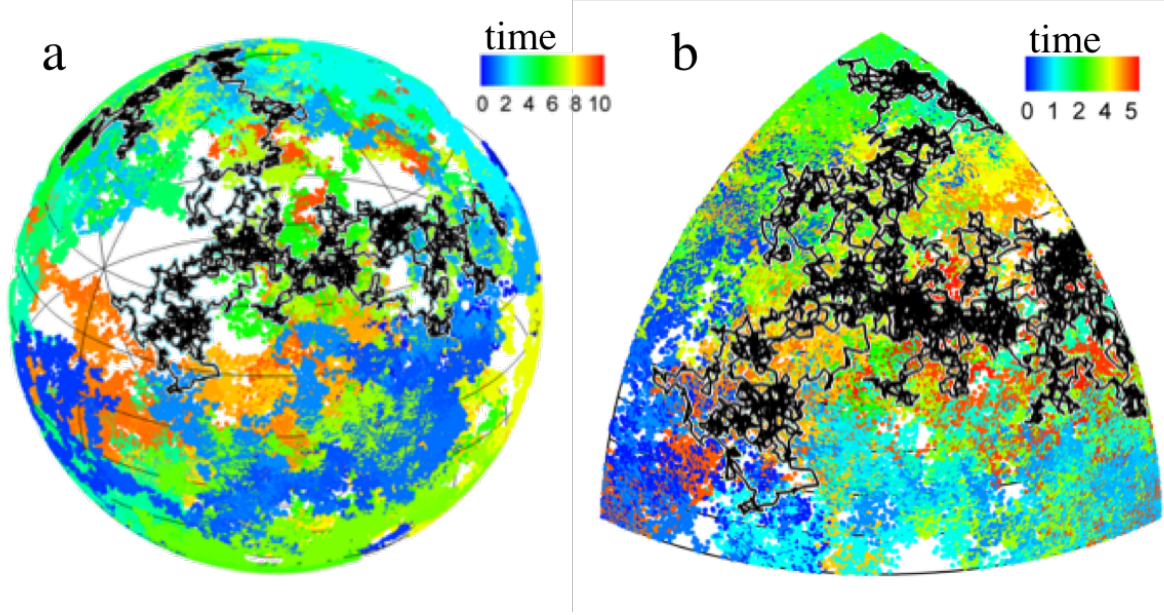


Figure S6: orientational trajectory of the Brownian nanorod. Location of $\hat{s}(t)$ is color coded by time. The black trajectory shows the orientation over 0.2s. a) Location of $\hat{s}(t)$ over a unit sphere and b) over an octant.

7. Control Calculation: Bounded translational random walk in 2D

As discussed in the main text the MSAD of the nanorod follows a stretched exponential function since the resolved orientation of the nanorod is bounded to an octant of a sphere. We report a model to map the bounded MSAD to an unbounded linearized MSAD, which works effectively in a viscous fluid. To verify the applicability of this model for MSAD of a GNR, suspended in a viscoelastic material, we develop here a toy model: an unbounded translational MSD of a Brownian particle diffusing in a viscoelastic material, which is then bounded by being transformed into a finite size square box. This model shows that the bounded MSD of the particle also follows a stretched exponential function, and that remapping back to an unbounded MSD recovers the correct result in the viscoelastic case.

To produce a random walk bounded to a box with finite dimension, we first generated a random walk in an unbounded space, $\vec{r}(x(t), y(t))$, shown as red line in Figure S7, and then we mirror reflect the simulated trajectory into the block box in the figure to produce a bounded trajectory $\vec{r}_b(x_b(t), y_b(t))$, shown by blue line in the same figure. The MSD of the unbounded trajectory $\langle \Delta r^2(t) \rangle = \langle |r(\tau + t) - r(\tau)|^2 \rangle_\tau$ is plotted by red squares in Figure S6, and the MSD of bounded trajectory, $\langle \Delta r_b^2(t) \rangle = \langle |r_b(\tau + t) - r_b(\tau)|^2 \rangle_\tau$, is shown by the blue circles. The asymptote of this curve can be derived by simple probability analysis. If we select

a set of pair of random points with uniform distribution inside a square with size b the average squared distance of the points of the pairs is $b^2/3$. This value is equivalent to the asymptote of the bounded MSD, i.e. $\langle \Delta r_b^2(\infty) \rangle$. Analogous to our findings with the bounded MSAD, we considered a stretched exponential function to model the bounded MSD as a function of unbounded MSD with the following from

$$\langle \Delta r_b^2(t) \rangle = \langle \Delta r_b^2(\infty) \rangle \left[1 - \exp \left(- \frac{1}{\langle \Delta r_b^2(\infty) \rangle} (\kappa \langle \Delta r^2(t) \rangle)^\lambda \right) \right], \quad (\text{S12})$$

where κ and λ are the fitting parameters. The blue solid line in Figure S7 shows the fitted curve based on equation 9 with the fitting parameters of $\kappa = 0.85$ and $\lambda = 0.95$. The inverse function of equation 9 is used to determine the unbounded MSD from the simulated or measured bounded MSD:

$$\langle \Delta r^2(t) \rangle = \frac{1}{\kappa} \left[- \langle \Delta r_b^2(\infty) \rangle \ln \left(1 - \frac{\langle \Delta r_b^2(t) \rangle}{\langle \Delta r_b^2(\infty) \rangle} \right) \right]^{1/\lambda}. \quad (\text{S13})$$

Generating bounded trajectories in boxes with different size shows that fitting parameter κ , and λ are independent of the size of the boxes, as expected. The blue dashed line in the Figure S7 shows the mapped MSD obtained from equation 10 which shows good overlap with the simulated unbounded MSD, red circles.

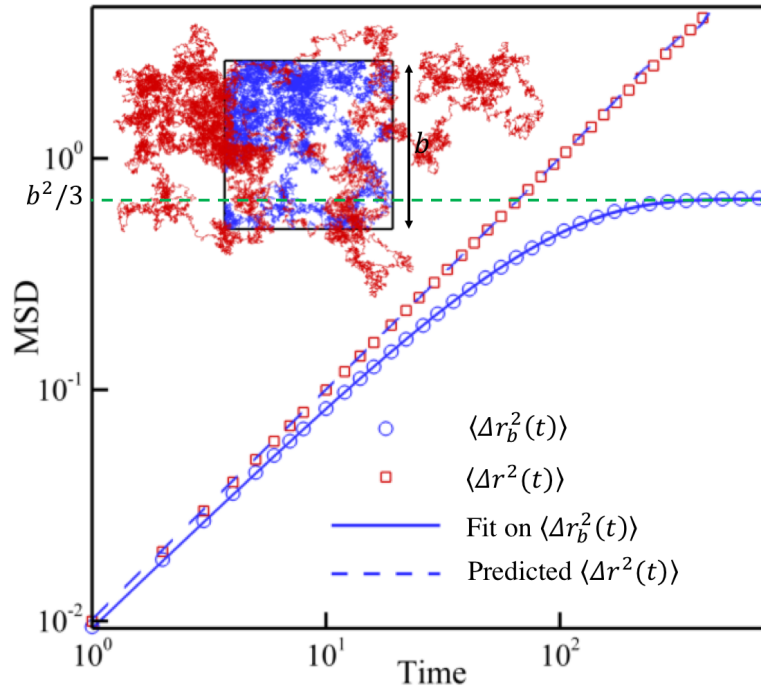


Figure S7 MSD of unbounded and bounded 2D trajectories. The red trajectory on the top left corner of the figure is representing random walk of a Brownian particle in infinite 2D space.

Blue trajectory is the projection of the red trajectory in a square box with size of $\sqrt{2}$. The open red squares are showing the MSD of the particle with red trajectory, and blue open circles are bounded MSD of the blue trajectory. Solid blue line is the fitted curve on the bounded MSD, and blue dashed line is mapped curved of bounded MSD on unbounded MSD. Green dashed line indicates the expected asymptote of the bounded MSD.

Now we need to verify that mapping function from bounded MSDs on unbounded MSDs, i.e. equation 10, is also valid for particles performing random walk in a non-Newtonian material. We first generated trajectories of particles in linear viscoelastic material based on the method provided by Khan and Mason [7,8]. We selected two materials as model viscoelastic media: power law fluids, and Maxwell-Voigt model (MVM). We then calculated unbounded and bounded MSD of the trajectories. The power law fluids have relaxation modulus of $G_r(t) \sim t^{-\alpha}$. Figure S8a shows the bounded MSDs of particle in several power law fluids with $\alpha = 0.1, 0.5, \text{ and } 0.9$ and a viscous fluid with $\alpha = 1$. Unbounded MSD of the same particles are plotted with open symbols in Figure S8b. Equation 10 is applied to map the bounded MSD to unbounded MSD, and the results are plotted with solid lines in Figure S8b which show good overlap with unbounded MSD.

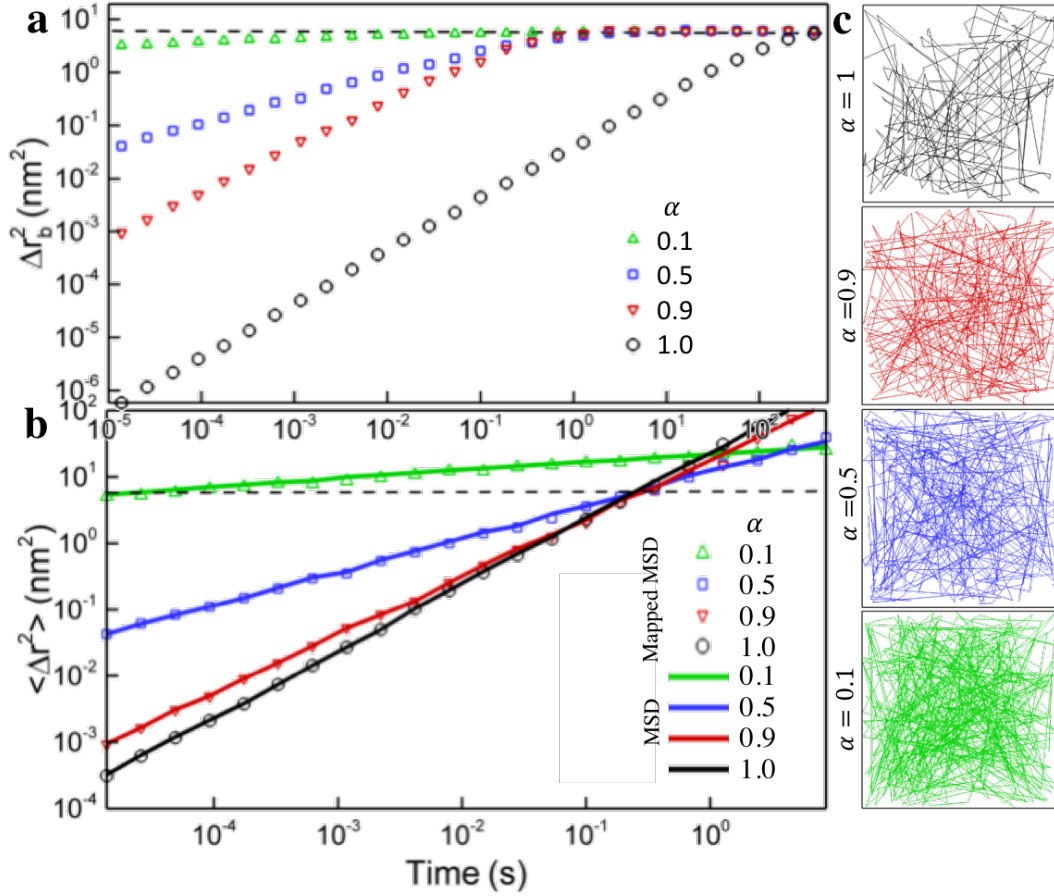


Figure S8 a) bounded MSD of power law fluids with different relaxation modulus. b) Line shows the simulated unbounded MSD of the power law fluids and open symbols are obtained by mapping the bounded MSDs plotted in (a). c) sub-trajectory of particles in four different power law fluids formed by 500 time steps.

For the second study case, we generated a trajectory of a spherical bead in a MVM media based on the method provided by Khan and Mason [7]. The MVM model provides a numerically challenging case for the integral transforms used in microrheology [7]; hence, it is a suitable case to test robustness of our mapping scheme. We choose identical parameters for MVM as in [7] to assure validity of the simulation. The low-frequency viscosity of the Maxwell part is $\eta_s^{MVM} = 10^4 Pa.s$, and the high-frequency viscosity of the Voigt part is $\eta_s^{MVM} = 10^{-3} Pa.s$. The matched elastic modulus of the both part is $G_p^{MVM} = 10^4 Pa$. The simulated trajectory of the MVM is shown in Figure S9a, and the MSD of the trajectory is plotted in Figure S9b. The MSD follows the theoretically predicted MSD, $\langle \Delta x^2(\tau) \rangle = 2D^{MVM}t + r_0^2[1 - \exp(-t/\tau_B)]$, where, D^{MVM} is the diffusion coefficient in long-time, r_0^2 is the plateau MSD, and τ_B is the crossover time. We then fold the trajectory inside several boxes

with different sizes relative to r_0 . The green trajectory which fills entire inset of Figure S9a is the folded trajectory with box size $b=1.6$ nm, while black line in the inset only represents 0.1% of the entire trajectory. The MSD of the bounded tracteries are plotted in Figure S9a with open symbols. We mapped bounded MSD using equation S13 and plotted them in Figure S9c with open symbols. Mapped MSDs for WLM show good agreement with the MSD of the unbounded trajectories.

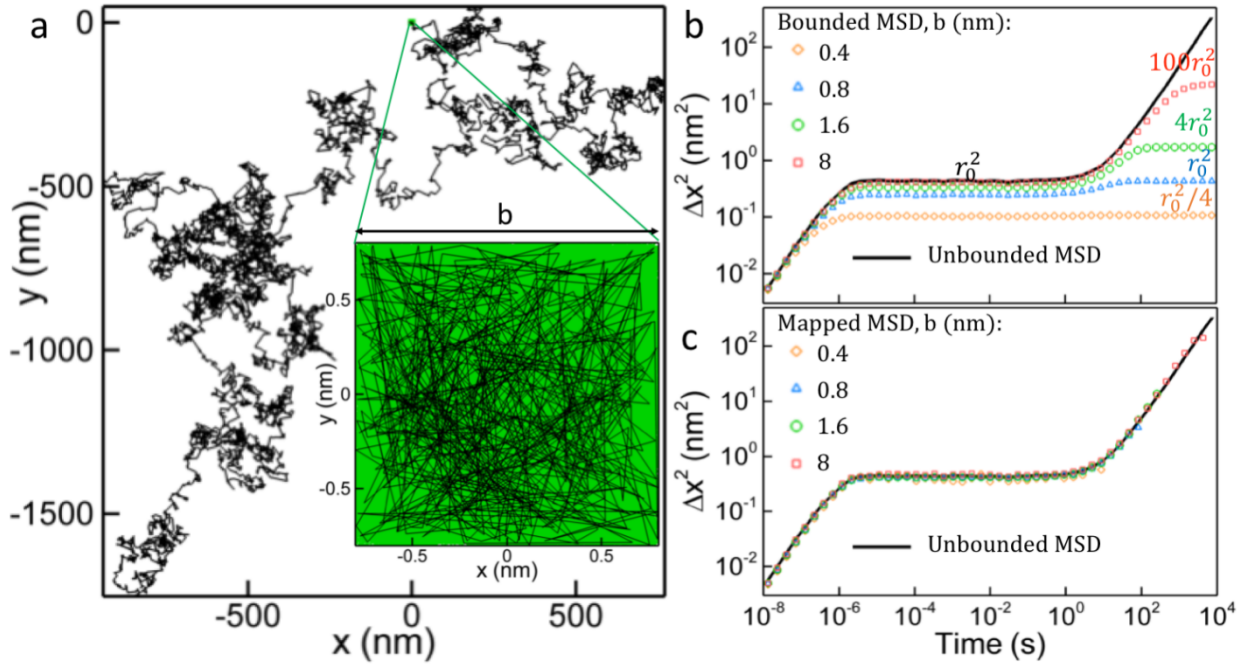


Figure S9 a) Simulated trajectory of $1\mu\text{m}$ spherical bead in MVM. Inset: folded trajectory in a box with size of 0.8 nm, green line, and portion of the folded trajectory formed by 500 times step, black line. b) solid line: MSD of unbounded trajectory shown in (a), open symbols: MSD of the bounded trajectory with different box sizes.

8. Rod drag coefficient model

To determine the diffusion coefficients, nanorods have been modeled as a spherocylinder or a cylinder with flat ends. The diffusion coefficients of a spherocylinder have been expressed as power series of its aspect ratio [9]:

$$D_t = \frac{k_B T}{3\pi\eta l} (\ln \rho + 0.386 + 0.6863\rho^{-1} - 0.0625\rho^{-2} - 0.01042\rho^{-3} - 0.000651\rho^{-4}) \quad (\text{S14a})$$

$$D_r = \frac{3k_B T}{\pi\eta l^3} \left(\ln \rho + 2 \ln 2 - \frac{11}{6} + \frac{\ln 2}{\ln(1+\rho)} \left[\frac{1}{3} - 2 \ln 2 + \frac{11}{6} - \sum a_i \right] + a \cdot \Omega \right), \quad (\text{S14b})$$

where $a = [13.04468, -62.6084, 174.0921, -218: 8365, 140.26992, -33.27076]$ and $\Omega = [\rho^{-1/4}, \rho^{-2/4}, \rho^{-3/4}, \rho^{-1}, \rho^{-5/4}, \rho^{-6/4}]$.

For a cylinder with flat ends the theoretical prediction for diffusion coefficients are [10,11]

$$D_t = \frac{k_B T}{3\pi\eta l} (\ln \rho + 0.316 + 0.5825\rho^{-1} + 0.05\rho^{-2}), \quad (\text{S15a})$$

$$D_r = \frac{3k_B T}{\pi\eta l^3} (\ln \rho - 0.662 + 0.917\rho^{-1} - 0.05\rho^{-2}). \quad (\text{S15b})$$

Knowing both translational and rotational diffusion coefficients of the nanorod and its diameter, one can determine its aspect ratio without knowing the physical parameters of the solution $\rho = f\left(\frac{1}{d^2} \frac{D_t}{D_r}\right)$. Figure S10 shows the shapes of this function for a spherocylinder and a cylinder with flat ends.

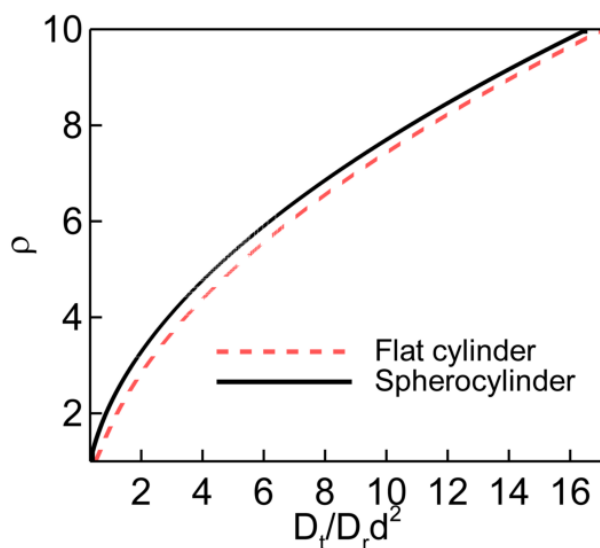


Figure S10 The aspect ratio of the flat cylinder and spherocylinder versus normalized ratio of translational to rotational diffusion coefficient based on the model provide by [10,11]

9. Dynamic error correction

Dynamic error is the deviation of measured particle MSD from the true MSD due to a finite exposure time of the camera. While there exist models to estimate the effect of dynamic error in the apparent MSD of the particle in simple Newtonian fluids and some simple non-Newtonian fluids such as power law and Voigt fluids [12] there is no such model for MSD of particles in general linear viscoelastic fluids. However, one can estimate the effect of the dynamic error by comparing the MSD at different exposure times. Here we recorded the angular motion of a GNR in 6.7 wt% PEO solution at three different exposure times $\sigma = 200, 150,$ and $100 \mu\text{s}$. We then determined the MSAD of the GNR using each exposure time, shown as dashed colored line in Figure S11. To determine and empirically remove the dynamic error

from the MASD measurement, we estimate the MSAD at a given lag time by linearly extrapolating of the MSAD values of each curve at that lag time versus exposure time to the value expected for zero exposure time. The extrapolated scaled MSAD is plotted by black dashed line in Figure S11 showing good agreement with scaled MSD of a spherical bead [13].

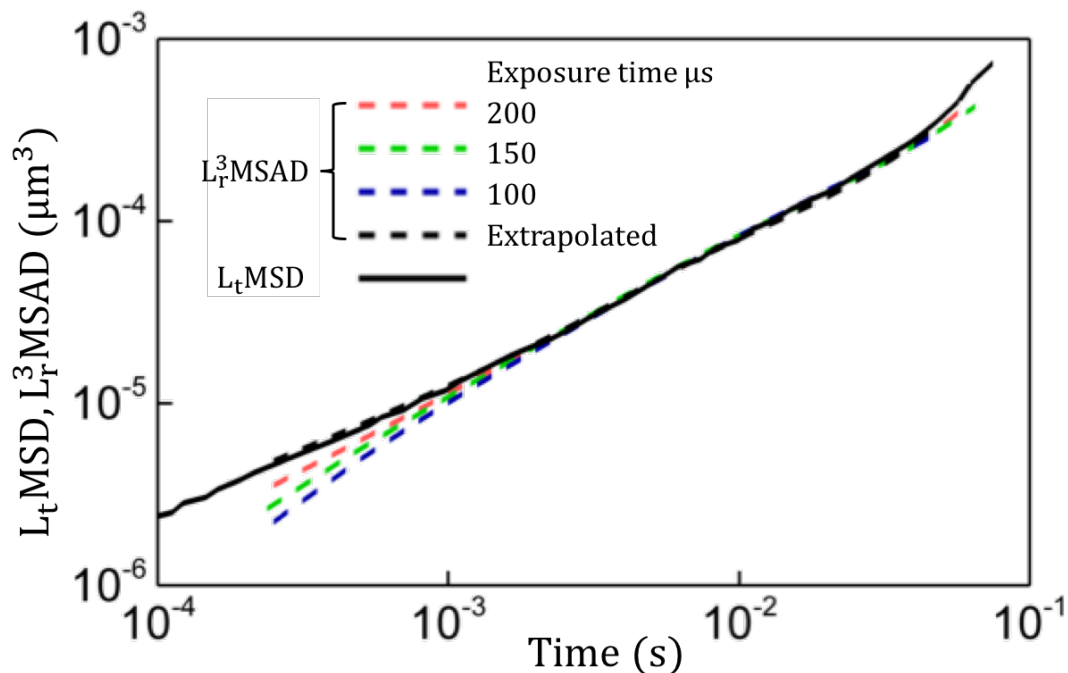


Figure S11: Scaled MSD and MSAD of particles in 6.7 wt % PEO solution. Colored dashed line: scaled MSAD of GNR recorded with three different exposure time. Black dashed line: extrapolated MSAD at zero exposure time. Black line are scaled MSD of the spherical bead from [13].

10. Anisotropic diffusion in viscoelastic media

Here we provide details of a Perrin-Lubensky type model to calculate the anisotropic-to-isotropic diffusion crossover and apparent cross-correlations between rotational and translational diffusion. We keep the derivation of the equations as general as possible to model the diffusion of an arbitrary non-chiral object with three orthogonal anisotropy axes. We start with anisotropic diffusion in a viscous fluid. We then derive general equations to model its motion in a viscoelastic fluid. At the end, we can evaluate this general case for uniaxial particles such as GNRs in our experiment.

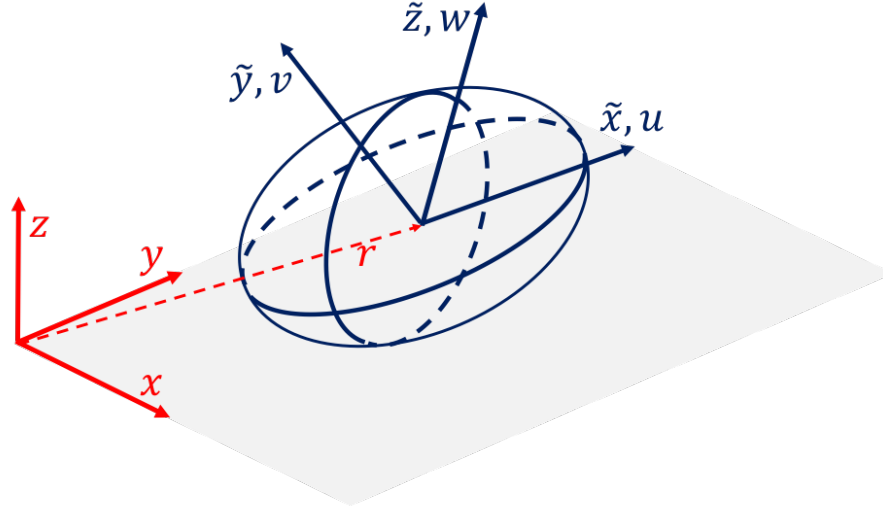


Figure S12: Illustration of a biaxial particle in the lab frame and moving body frame.

The orientation of the particle in the fixed lab frame is identified with three orthogonal principal vectors, u , v , and w sitting on the particle and forming a moving body frame as shown in Figure S12. We identify the position of the particle in the fixed lab frame with vector $r(t) = [x(t), y(t), z(t)]$ and in the body frame with $\tilde{r}(t) = [\tilde{x}, \tilde{y}, \tilde{z}]$. The translational, $\tilde{\Gamma}_{ij}$ and rotational, $\tilde{\Gamma}_{ij}^r$ mobility tensor in the body frame for a non-chiral particle are diagonal tensors:

$$\tilde{\Gamma}_{ij} = \begin{bmatrix} \Gamma_u & 0 & 0 \\ 0 & \Gamma_v & 0 \\ 0 & 0 & \Gamma_w \end{bmatrix} = \begin{bmatrix} \gamma_u^{-1} & 0 & 0 \\ 0 & \gamma_v^{-1} & 0 \\ 0 & 0 & \gamma_w^{-1} \end{bmatrix} = \frac{1}{G_r(t)} \begin{bmatrix} \Pi_u & 0 & 0 \\ 0 & \Pi_v & 0 \\ 0 & 0 & \Pi_w \end{bmatrix} \quad (16a)$$

$$\tilde{\Gamma}_{ij}^\theta = \begin{bmatrix} \Gamma_u^\theta & 0 & 0 \\ 0 & \Gamma_v^\theta & 0 \\ 0 & 0 & \Gamma_w^\theta \end{bmatrix} = \begin{bmatrix} \gamma_u^{\theta-1} & 0 & 0 \\ 0 & \gamma_v^{\theta-1} & 0 \\ 0 & 0 & \gamma_w^{\theta-1} \end{bmatrix} = \frac{1}{G_r(t)} \begin{bmatrix} \Pi_u^\theta & 0 & 0 \\ 0 & \Pi_v^\theta & 0 \\ 0 & 0 & \Pi_w^\theta \end{bmatrix}, \quad (16b)$$

where γ_q and γ_q^θ are translational and rotational drag coefficient along vector \hat{q} , and Π_q and Π_q^θ are frequency independent mobility tensor, and $G_r(t)$ is the stress relaxation modulus. In the case of a viscous fluid, stress relaxation modulus is identical to the viscosity, $G_r(t) = \eta$. The mobility tensor in the fixed lab frame can be determined based on $\tilde{\Gamma}_{ij}$ and $\tilde{\Gamma}_{ij}^r$ and the orientation vectors as $\Gamma_{ij}(U(t)) = (U^T \tilde{\Gamma} U)_{ij}$, where $U_{ij}(t) = [u(t) \ v(t) \ w(t)]$ is the orientation tensor.

The translational and rotational Langevin equations in the lab frame are expressed as following:

$$\partial_t r_i = -\Gamma_{ij}(U) \frac{\partial H}{\partial x_j} + \xi_i(t), \quad (\text{S17a})$$

$$\partial_t \theta_i = -\Gamma_{ij}^\theta(U) \frac{\partial H}{\partial \theta_j} + \xi_i^\theta(t), \quad (\text{S17b})$$

where the Hamiltonian H describes the external forces and torques. The mobility tensor Γ_{ij} is expressed as sum of four terms $\Gamma_{ij} = \bar{\Gamma} \delta_{ij} + (\Gamma_u - \Gamma_v) M_{ij}^{uv} + (\Gamma_u - \Gamma_w) M_{ij}^{uw} + (\Gamma_v - \Gamma_w) M_{ij}^{vw}$ where $\bar{\Gamma} = \frac{1}{3}(\Gamma_u + \Gamma_v + \Gamma_w)$ and

$$M_{ij}^{pq} = \begin{bmatrix} \frac{1}{3}(p_x^2 - q_x^2) & \frac{1}{2}(p_x p_y - q_x q_y) & \frac{1}{2}(p_x p_z - q_x q_z) \\ \frac{1}{2}(p_x p_y - q_x q_y) & \frac{1}{3}(p_y^2 - q_y^2) & \frac{1}{2}(p_y p_z - q_y q_z) \\ \frac{1}{2}(p_x p_z - q_x q_z) & \frac{1}{2}(p_y p_z - q_y q_z) & \frac{1}{3}(p_z^2 - q_z^2) \end{bmatrix}. \quad (\text{S18})$$

In the absence of the external forces and torques the Langevin equations S12a&b are simplified to $\partial_t r_i = \xi_i(t)$ and $\partial_t \theta_i = \xi_i^\theta(t)$. Where $\xi_i(t)$ and $\xi_i^\theta(t)$ are Gaussian random variables with time dependent variances

$$\langle \xi_i(t) \xi_i(t') \rangle = 2k_B T \Gamma_{ij}(U) \delta(t - t'), \quad (\text{S19a})$$

$$\langle \xi_i(t) \xi_i(t') \rangle = 2k_B T \Gamma_{ij}^\theta(U) \delta(t - t'). \quad (\text{S19b})$$

Applying these random noise terms to the Langevin equations, translational and angular displacements can be determined

$$\langle \Delta r_i(t) \Delta r_j(t) \rangle_{U0} = \int_0^t dt_1 \int_0^t dt_2 \langle \xi_i(t_1) \xi_j(t_2) \rangle_{U0}^{\xi_i \xi_j} = \int_0^t 2k_B T \langle \Gamma_{ij}(U) \rangle_{U0}^{\xi_i \xi_j} dt_1 \quad (\text{S20a})$$

$$\langle \Delta \theta_i(t) \Delta \theta_j(t) \rangle_{U0} = \int_0^t dt_1 \int_0^t dt_2 \langle \xi_i^\theta(t_1) \xi_j^\theta(t_2) \rangle_{U0}^{\xi_i \xi_j} = \int_0^t dt_1 2k_B T \langle \Gamma_{ij}^\theta(U) \rangle_{U0}^{\xi_i \xi_j}. \quad (\text{S20b})$$

Where $\langle \dots \rangle_{U0}^{\xi_i \xi_j}$ indicates that ξ_U are being averaged at fixed initial orientation $U(0)$. Since both correlations in angular and translational displacement depend on the orientation of the object we first consider properties of $U(t)$. The change in the orientation tensor can be considered by three rotations with small angles around three fixed orthogonal axes in the lab frame, $U(t + dt) = R_{xyz} U(t)$, Where R_{xyz} is the rotation tensor around $x, y, \text{ and } z$ axes assuming small angle rotation

$$R_{xyz} \approx \begin{bmatrix} c_y c_z & -s_z & s_y \\ s_z & c_x c_z & -s_x \\ -s_y & s_x & c_x c_y \end{bmatrix}, \quad (\text{S21})$$

where $c_q = \cos \Delta \theta_q(dt)$ and $s_q = \sin \Delta \theta_q(dt)$ are the sin and cos of the rotation angle around vector \hat{q} and $\Delta \theta_q(dt) = \xi_q^\theta(t) dt$. Rotating orientation tensor $U(t)$ with R_{xyz} leads to:

$$U_{ix}(t + dt) = c_y c_z U_{ix}(t) - s_z U_{iy}(t) + s_y U_{iz}(t). \quad (S22)$$

Taking average of the square of both side of equation (S19) leads to:

$$\langle U_{ix}(t + dt)^2 \rangle = \langle c_y^2 \rangle \langle c_z^2 \rangle \langle U_{ix}^2(t) \rangle + \langle s_z^2 \rangle \langle U_{iy}^2 \rangle + \langle s_y^2 \rangle \langle U_{iz}^2 \rangle. \quad (S23)$$

Assuming an infinitesimal rotation angle, $\Delta\theta \ll 1$, and applying the following binomial expansions, $\cos^n \Delta\theta \approx 1 - \frac{n\Delta\theta^2}{2}$, $\sin^n \Delta\theta \approx \Delta\theta^n$ gives to:

$$\langle U_{ix}^2(t + dt) \rangle - \langle U_{ix}^2(t) \rangle = - \left(\Delta\theta_y^2(dt) + \Delta\theta_z^2(dt) \right) \langle U_{ix}^2(t) \rangle + \Delta\theta_z^2(dt) \langle U_{iy}^2(t) \rangle + \Delta\theta_y^2(dt) \langle U_{iz}^2(t) \rangle. \quad (S24)$$

Now we rewrite equation (S17a&b) in terms of frequency independent mobility tensor and stress relation modulus

$$\langle \Delta\theta_i(t) \Delta\theta_j(t) \rangle_{U_0} = 2k_B T \int_0^t \frac{\langle \Pi_{ij}^\theta(U(t')) \rangle_{U_0}}{G_r(t')} dt' \quad (S25a)$$

$$\langle \Delta r_i(t) \Delta r_j(t) \rangle_{U_0} = 2k_B T \int_0^t \frac{\langle \Pi_{ij}(U(t')) \rangle_{U_0}}{G_r(t')} dt'. \quad (S25b)$$

These Equations can be expressed in simpler form in terms of the creep compliance function:

$$\langle \Delta\theta_i(J) \Delta\theta_j(J) \rangle_{U_0} = 2k_B T \int_0^J \langle \Pi_{ij}^\theta(U(J')) \rangle_{U_0} dJ' \quad (S26a)$$

$$\langle \Delta r_i(J) \Delta r_j(J) \rangle_{U_0} = 2k_B T \int_0^J \langle \Pi_{ij}(U(J')) \rangle_{U_0} dJ', \quad (S26b)$$

where $J = t/G_r(t)$. If instead of taking average at fixed initial orientation, we take the average over entire initial orientation in equation (S23b) we can determine the creep compliance function based on the MSAD

$$\langle \Delta\theta_i^2(t) \rangle = 2k_B T \Pi^\theta J(t). \quad (S27)$$

Therefore, to determine anisotropic-to-isotropic crossover in a viscoelastic material, we derive the equation at different MSAD and then map the equation to the time domain based on the creep compliance. Thus, we form a differential equation to evaluate orientation vector over the time using equation (S24):

$$\frac{d}{dJ} \langle U_{ix}^2(J) \rangle = -2k_B T \left(\langle \Pi_{jy}(U(J)) \rangle_{U_0} + \langle \Pi_{jx}(U(J)) \rangle_{U_0} \right) \langle U_{ix}^2(J) \rangle_{U_0} + 2k_B T \langle \Pi_{jy}(U(J)) \rangle_{U_0} \langle U_{iz}^2(J) \rangle_{U_0} + 2k_B T \langle \Pi_{jz}(U(J)) \rangle_{U_0} \langle U_{iy}^2(J) \rangle_{U_0}. \quad (S28)$$

Equation S25 is a system of nonlinear differential equations which can be solved using different numerical scheme such as Runge-Kutta method. For instance, Figure S13 shows the

crossover of $\langle u_i^2 \rangle$ as function of time for the case where $\Pi_u^\theta = 2\Pi_v^\theta = 10\Pi_w^\theta = 0.1 \text{ rad}^2/\text{s}$. After solving equation S25 we use $\langle U_{ij}^2(J) \rangle$ in equation S23b to determine $\langle \Delta x_i(J) \Delta x_j(J) \rangle_{u_0}$.

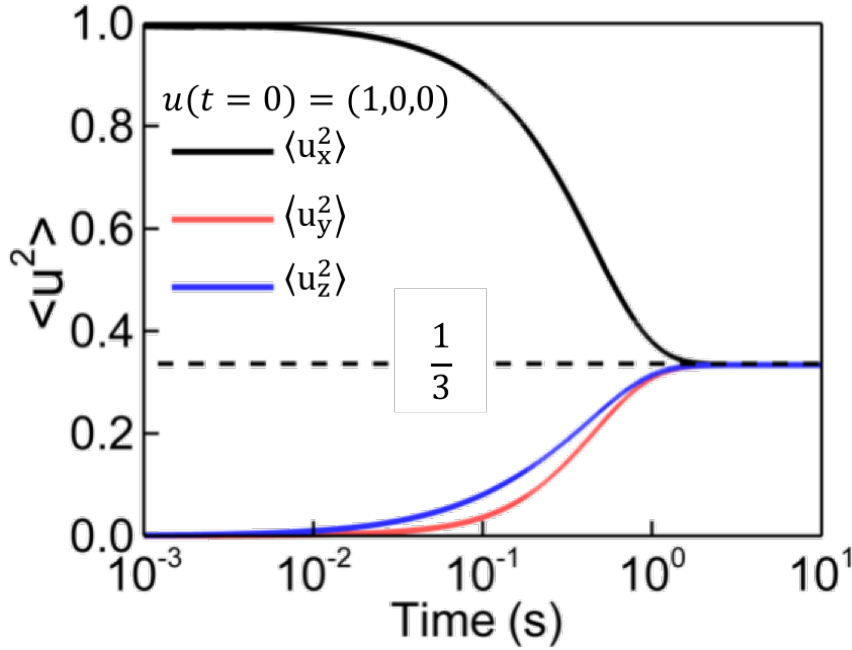


Figure S13: crossover of $\langle u_i^2 \rangle$ as function of time at fixed initial orientation $u(0) = e_x$ for a particle with $\Pi_u^\theta = 2\Pi_v^\theta = 10\Pi_w^\theta = 0.1 \text{ rad}^2/\text{s}$

11. Anisotropic-to-isotropic diffusion in a viscous fluid

Contrary to the case of a viscoelastic material, in the viscous fluid, we can determine the change in the orientation tensor by three rotations with small angles around three principal axes of the particle. This simplifies the derivation of equation since it linearizes the nonlinear system of equations S25. The rotation matrix for rotating a vector u around two orthogonal vectors v and w with infinitesimal angles is

$$R_{vw} = c_v c_w I + c_v s_w \begin{bmatrix} 0 & -w_z & w_y \\ w_z & 0 & -w_x \\ -w_y & w_x & 0 \end{bmatrix} + s_v c_w \begin{bmatrix} 0 & -v_z & v_y \\ v_z & 0 & -v_x \\ -v_y & v_x & 0 \end{bmatrix}. \quad (\text{S29})$$

Rotating $u(t)$ with R_{vw} , $v(t)$ with R_{uw} , and $w(t)$ with R_{vu} leads to:

$$u_i(t + dt) = c_v c_w u_i + c_v s_w v_i - s_v c_w w_i \quad (\text{S30a})$$

$$v_i(t + dt) = c_u c_w v_i - c_u s_w u_i + c_w s_u w_i \quad (\text{S30b})$$

$$w_i(t + dt) = c_u c_v w_i + c_u s_v u_i - c_v s_u v_i, \quad (\text{S30c})$$

where $c_k = \cos \tilde{\theta}_k \approx 1 - \frac{\tilde{\theta}_k^2}{2}$ and $s_k = \sin \tilde{\theta}_k \approx \tilde{\theta}_k$. Taking average from square of terms in both sides of equation (S27) at fixed initial orientation $U0$ leads to the system of linear differential equations:

$$\frac{d}{dt} \langle u_i(t)^2 \rangle = -3(D_v^\theta + D_w^\theta) \langle u_i(t)^2 \rangle + (D_w^\theta - D_v^\theta) (\langle v_i(t)^2 \rangle - \langle w_i(t)^2 \rangle) + (D_w^\theta + D_v^\theta) \quad (\text{S31a})$$

$$\frac{d}{dt} \langle v_i(t)^2 \rangle = -3(D_w^\theta + D_u^\theta) \langle v_i(t)^2 \rangle + (D_u^\theta - D_w^\theta) (\langle w_i(t)^2 \rangle - \langle u_i(t)^2 \rangle) + (D_u^\theta + D_w^\theta) \quad (\text{S31b})$$

$$\frac{d}{dt} \langle w_i(t)^2 \rangle = -3(D_v^\theta + D_u^\theta) \langle w_i(t)^2 \rangle + (D_v^\theta - D_u^\theta) (\langle u_i(t)^2 \rangle - \langle v_i(t)^2 \rangle) + (D_v^\theta + D_u^\theta), \quad (\text{S31c})$$

where $D_q^\theta = k_B T \Gamma_q^\theta$ is the rotation diffusion constant around the axis q . Before solving these equations, we note that $\frac{d}{dt} \langle u(t)^2 \rangle + \frac{d}{dt} \langle v(t)^2 \rangle + \frac{d}{dt} \langle w(t)^2 \rangle = 0$ as expected. Therefore, we reduce the order of the system to 2 by substituting $\langle w(t)^2 \rangle = 1 - \langle u(t)^2 \rangle - \langle v(t)^2 \rangle$ and form the following system of equation

$$\frac{d}{dt} \begin{bmatrix} \langle u_i(t)^2 \rangle \\ \langle v_i(t)^2 \rangle \end{bmatrix} = A \begin{bmatrix} \langle u_i(t)^2 \rangle \\ \langle v_i(t)^2 \rangle \end{bmatrix} + \begin{bmatrix} 2D_v^\theta \\ 2D_u^\theta \end{bmatrix},$$

where

$$A = -2 \begin{bmatrix} 2D_v^\theta + D_w^\theta & D_v^\theta - D_w^\theta \\ D_u^\theta - D_w^\theta & 2D_u^\theta + D_w^\theta \end{bmatrix}.$$

Particular solution for the system of equation is $\langle u_i(t)^2 \rangle_p = \langle v_i(t)^2 \rangle_p = 1/3$. The eigenvalues and the eigenvectors of matrix A are

$$\lambda_1 = -6(D^\theta + \Delta D^\theta), \quad \lambda_2 = -6(D^\theta - \Delta D^\theta)$$

$$\chi_1 = \begin{bmatrix} D_w^\theta - D_v^\theta \\ D_v^\theta - D_u^\theta - 3\Delta D_r \end{bmatrix} \text{ and } \chi_2 = \begin{bmatrix} D_w^\theta - D_v^\theta \\ D_v^\theta - D_u^\theta + 3\Delta D_r \end{bmatrix},$$

where $D_r = \frac{1}{3}(D_u^\theta + D_v^\theta + D_w^\theta)$, $\Delta D_r = \sqrt{D_r^2 - D_r^*}$, and $D_r^* = \frac{1}{3}(D_u^\theta D_v^\theta + D_u^\theta D_w^\theta + D_v^\theta D_w^\theta)$.

After applying the initial conditions, particular solutions, and introducing variables $D_r^- = D_r - \Delta D_r$ and $D_r^+ = D_r + \Delta D_r$, we get the following form for the mean square of the orientation vector:

$$\langle u_i(t)^2 \rangle = \frac{1}{3} + \left(u_i^2(0) - \frac{1}{3} \right) \frac{(D_u^\theta - D_r + 2\Delta D_r)}{4\Delta D_r} \exp(-6D_r^- t) + \left(u_i^2(0) - \frac{1}{3} \right) \frac{(D_r - D_u^\theta + 2\Delta D_r)}{4\Delta D_r} \exp(-6D_r^+ t) + \left(v_i^2(0) - w_i^2(0) \right) \frac{(D_w^\theta - D_v^\theta)}{12\Delta D_r} [\exp(-6D_r^- t) - \exp(-6D_r^+ t)]. \quad (\text{S32})$$

With the preceding formulae for orientation vector, now we calculate the correlations in translational displacement $r(t)$. We begin with equation (S17b) expressing the second moment:

$$\langle \Delta r_i^2(t) \rangle_{U0} = 2\bar{D}t + 2\Delta D_{uv} \int_0^t dt_1 \langle M_{ii}^{uv}(t_1) \rangle_{U0} + 2\Delta D_{uw} \int_0^t dt_1 \langle M_{ii}^{uw}(t_1) \rangle_{U0} + 2\Delta D_{vw} \int_0^t dt_1 \langle M_{ii}^{vw}(t_1) \rangle_{U0}, \quad (\text{S33})$$

where $\Delta D_{qp} = D_q - D_p$ and $D_q = k_B T \Gamma_q$. We first calculate the integral terms, $\int_0^t dt_1 \langle M_{ii}^{uv}(t_1) \rangle_{U0}$ in equation S30:

$$\int_0^t \langle M_{ii}^{uv}(t') \rangle_{U0} dt' = \frac{1}{6\Delta D_r} \left[\left(u_i^2(0) - \frac{1}{3} \right) D_u^\theta - \left(v_i^2(0) - \frac{1}{3} \right) D_v^\theta - D_r^- \left(u_i^2(0) - v_i^2(0) \right) \right] \tau^- + \frac{1}{6\Delta D_r} \left[- \left(u_i^2(0) - \frac{1}{3} \right) D_u^\theta + \left(v_i^2(0) - \frac{1}{3} \right) D_v^\theta + D_r^+ \left(u_i^2(0) - v_i^2(0) \right) \right] \tau^+, \quad (\text{S34})$$

where τ^- and τ^+ are the following time functions:

$$\tau^- = \int_0^t \exp(-6D_r^- t') dt' = \frac{1 - \exp(-6D_r^- t)}{6D_r^-} \quad (\text{S35a})$$

$$\tau^+ = \int_0^t \exp(-6D_r^+ t') dt' = \frac{1 - \exp(-6D_r^+ t)}{6D_r^+}. \quad (\text{S35b})$$

Replacing equation S32 in equation S31 leads to:

$$D_{ii} = \bar{D} + \frac{\tau^-}{6\Delta D_r t} \left[\left(u_i^2(0) - \frac{1}{3} \right) (D_u - \bar{D})(D_u^\theta - D_r^-) + \left(v_i^2(0) - \frac{1}{3} \right) (D_v - \bar{D})(D_v^\theta - D_r^-) + \left(w_i^2(0) - \frac{1}{3} \right) (D_w - \bar{D})(D_w^\theta - D_r^-) \right] + \frac{\tau^+}{6\Delta D_r t} \left[\left(u_i^2(0) - \frac{1}{3} \right) (D_u - \bar{D})(D_r^+ - D_u^\theta) + \left(v_i^2(0) - \frac{1}{3} \right) (D_v - \bar{D})(D_r^+ - D_v^\theta) + \left(w_i^2(0) - \frac{1}{3} \right) (D_w - \bar{D})(D_r^+ - D_w^\theta) \right]. \quad (\text{S36})$$

Equation S33 expresses the anisotropic-to-isotropic crossover of diffusion in 3D for an object with three anisotropy axes. For a uniaxial object such as a GNR with translation diffusion coefficients D_{\parallel} and D_{\perp} parallel and normal to major axis of GNR respectively and rotation diffusion of D_r , equation S33 attains a simpler form:

$$D_{ii} = \frac{\langle \Delta r_i^2 \rangle}{2t} = \bar{D} + \Delta D \left(u_i^2(0) - \frac{1}{3} \right) \frac{\tau}{t}, \quad (\text{S37})$$

where $\bar{D} = (D_{\parallel} + 2D_{\perp})/3$, $\Delta D = D_{\parallel} - D_{\perp}$, and $\tau = (1 - \exp(-6D_r t))/6D_r$.

12. Physical characteristics of the polymer solutions

The mesh size of the polymer solution can be calculated by the following equation [14]

$$\xi = R_g(c^*/c)^{0.75}, \quad (\text{S38})$$

where R_g , c^* , and c are radius of gyration, overlap concentration, and concentration of the polymer respectively. R_g is estimated using following equation [14]

$$R_g = 0.215M_w^{0.583 \mp 0.031}, \quad (\text{S39})$$

where, M_w is the molecular weight of the polymer. For PEO with $M_w = 200\text{KDa}$, the radius of gyration is estimated as $R_g \approx 26 \text{ nm}$. Also, overlap concentration is related to the radius of gyration according to following equation [14]

$$c^* = \frac{3}{4} \frac{M_w}{\pi N_A R_g^3}, \quad (\text{S40})$$

where, N_A denotes the Avogadro's number. The overlap concentration for 200 KDa PEO solution is approximately 0.48 wt%. Therefore, using equation S38 the mesh size for the PEO solution with $c=6.7$ and 12 wt% is $\xi = 3.6$ and 2.3 nm respectively.

13. Non-normalized anisotropic MSD in PEO solution

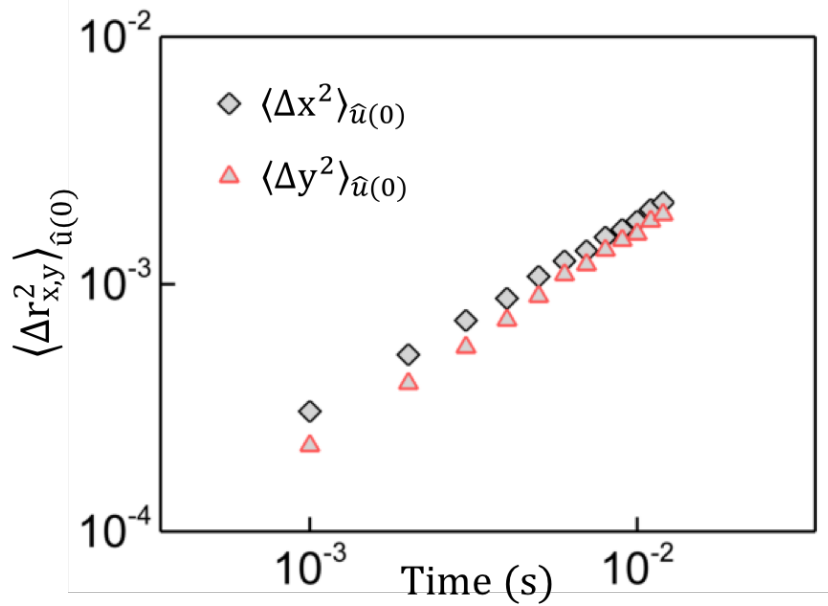


Figure S14: Non-normalized MSD of the GNR embedded in PEO 6.77 wt % solution in the lab frame with $\hat{u}(0) = \hat{e}_x$ corresponding to normalized MSD shown in figure 4e.

References

- [1] M. A. Yurkin and A. G. Hoekstra, *Journal of Quantitative Spectroscopy and Radiative Transfer* **112**, 2234 (2011).
- [2] E. M. Purcell and C. R. Pennypacker, *The Astrophysical Journal* **186**, 705 (1973).
- [3] P. B. Johnson and R.-W. Christy, *Physical review B* **6**, 4370 (1972).
- [4] H. Chen, L. Shao, Q. Li, and J. Wang, *Chem. Soc. Rev.* **42**, 2679 (2013).
- [5] J. C. Crocker and D. G. Grier, *J. Colloid Interface Sci.* **179**, 298 (1996).
- [6] D. Axelrod, *Biophys. J.* **26**, 557 (1979).
- [7] M. Khan and T. G. Mason, *Phys. Rev. E* **89**, 042309 (2014).
- [8] M. Khan and T. G. Mason, *Soft Matter* **10**, 9073 (2014).
- [9] I. Martchenko, H. Dietsch, C. Moitzi, and P. Schurtenberger, *J. Phys. Chem. B* **115**, 14838 (2011).
- [10] M. M. Tirado, C. L. Martínez, and J. G. de la Torre, *The Journal of chemical physics* **81**, 2047 (1984).
- [11] A. Wang, T. G. Dimiduk, J. Fung, S. Razavi, I. Kretzschmar, K. Chaudhary, and V. N. Manoharan, *Journal of Quantitative Spectroscopy and Radiative Transfer* **146**, 499 (2014).
- [12] T. Savin and P. S. Doyle, *Biophys. J.* **88**, 623 (2005).
- [13] B. R. Dasgupta, S.-Y. Tee, J. C. Crocker, B. Frisken, and D. Weitz, *Phys. Rev. E* **65**, 051505 (2002).
- [14] I. Teraoka, *Frontmatter and Index* (Wiley Online Library, 2002).